AD-A130 889 HIGH-LATITUDE F-REGION IRREGULARITIES: INTENSITY AND SCALE SIZE DISTRIBUTIONS(U) NAVAL RESEARCH LAB WASHINGTON DC P RODRIGUEZ ET AL. 21 JUL 83 NRL-MR-5120 1/1

UNCLASSIFIED F/G 4/1 NL

END
DATE
FILMED
9 83
DTIC

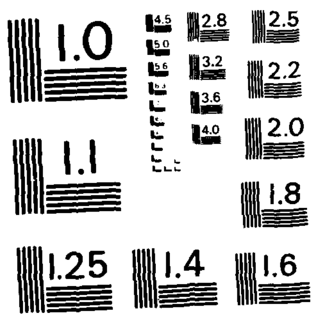

MICROCOPY RESOLUTION TEST CHART
NATIONAL BUREAU OF STANDARDS-1963-A

SECURITY CLASSIFICATION OF THIS PAGE (When Data Entered)

REPORT DOCUMENTATION PAGE

READ INSTRUCTIONS BEFORE COMPLETING FORM

1. REPORT NUMBER: NRL Memorandum Report 5120	2. GOVT ACCESSION NO.: AD-A130	3. RECIPIENT'S CATALOG NUMBER: 889
4. TITLE (and Subtitle): HIGH-LATITUDE F-REGION IRREGULARITIES: INTENSITY AND SCALE SIZE DISTRIBUTIONS		5. TYPE OF REPORT & PERIOD COVERED: Interim report on a continuing NRL problem.
		6. PERFORMING ORG. REPORT NUMBER
7. AUTHOR(s): P. Rodriguez and E.P. Szuszczewicz		8. CONTRACT OR GRANT NUMBER(s)
9. PERFORMING ORGANIZATION NAME AND ADDRESS: Naval Research Laboratory Washington, DC 20375		10. PROGRAM ELEMENT, PROJECT, TASK AREA & WORK UNIT NUMBERS: 62715H; RR033-02-44; 41-0949-0-3
11. CONTROLLING OFFICE NAME AND ADDRESS: Office of Naval Research Arlington, VA 22217; Defense Nuclear Agency Washington, DC 20305		12. REPORT DATE: July 21, 1983
		13. NUMBER OF PAGES: 54
14. MONITORING AGENCY NAME & ADDRESS (if different from Controlling Office)		15. SECURITY CLASS. (of this report): UNCLASSIFIED
		15a. DECLASSIFICATION/DOWNGRADING SCHEDULE

16. DISTRIBUTION STATEMENT (of this Report)

Approved for public release; distribution unlimited.

17. DISTRIBUTION STATEMENT (of the abstract entered in Block 20, if different from Report)

18. SUPPLEMENTARY NOTES

This report was partially sponsored by the Defense Nuclear Agency under Subtask I25AAXHX, work unit 00014, work unit title "Nuclear Weapons Effects Program," and the Office of Naval Research.

19. KEY WORDS (Continue on reverse side if necessary and identify by block number)

High-latitude F-region irregularities
Scale size distributions
Polar cusp
Auroral oval

20. ABSTRACT (Continue on reverse side if necessary and identify by block number)

A broad range of lower F-region irregularity scale sizes (150 km > L > 75m) at high northern latitudes during the spring and summer of 1978 has been studied. The morphology and intensity distribution of the irregularities shows that particle precipitation in the auroral oval and polar cusp are the primary agents in driving density fluctuations. The most intense density fluctuations observed under moderately active

(Continues)

DD FORM 1 JAN 73 1473 EDITION OF 1 NOV 65 IS OBSOLETE
S/N 0102-014-6601

SECURITY CLASSIFICATION OF THIS PAGE (When Data Entered)

20 ABSTRACT (Continued)

geomagnetic conditions (Kp $\leqslant$ 2-3, AE $\sim$ 100) occur in the polar cusp, where small scale irregularities (L $\geqslant$ 75m) are particularly prominent. Absolute density enhancements approaching 10^6 cm^{-3} have been observed in the polar cusp. Auroral oval irregularities have absolute density enhancements generally less than the polar cusp enhancements, with maximum values of about 8×10^5 cm^{-3}. Large density enhancements within the polar cap have been detected principally toward the duskward side. These polar cap enhancements are similar to auroral oval enhancements, thus suggesting that polar cap precipitation is the source of the density fluctuations. A region of density depletion with respect to the background photoionization is found toward the dawnward side of the polar cap. Such relative depletions may arise from the joint action of lower F-region recombination rates and enhanced cross-field diffusion. In general, the overall two-cell convection pattern at high latitudes has a minimal effect in the redistribution of precipitation-induced irregularities.

CONTENTS

HIGH-LATITUDE F-REGION IRREGULARITIES: INTENSITY AND SCALE SIZE DISTRIBUTIONS

I. INTRODUCTION

A. The Latitudinal Regimes of F-Region Irregularities

The study of density irregularities in the ionospheric F-region has divided itself naturally into three regimes: the low, middle and high geomagnetic latitudes. These regimes have fundamentally different sources of the irregularities, associated with the degree of coupling to higher altitude magnetospheric phenomena. The coupling is related, of course, to the orientation of the geomagnetic field as a function of magnetic latitude.

At low latitudes, where the geomagnetic field tends to be horizontal, direct coupling to magnetospheric disturbances is inhibited since plasma motion is constrained to follow the magnetic field line direction. As a result, localized instabilities such as the Rayleigh-Taylor and $\bar{E} \times \bar{B}$ gradient drift instabilities are the principal sources of low latitude F-region irregularities. The study of the nighttime phenomenon called equatorial spread-F is an example of a relatively extensive investigation of local plasma instability processes in the F-region ionosphere. Theoretical and experimental efforts have identified cause-effect relationships for irregularity distributions extending from planetary scale sizes (tens-to-hundreds of kilometers) down to the short-wavelength sub-meter regime (Kelley [1979]; Fejer and Kelley [1980]; Ossakow [1979]; Keskinen et al. [1981]; Szuszczewicz et al. [1981]; Kelley et al. [1982b]; and Singh and Szuszczewicz [1983]). In many ways, the equatorial study and attendant definitions of irregularity scale size

Manuscript approved May 6, 1983.

domains has laid a valuable foundation for its more complicated counterpart at high latitudes.

Generally, the mid-latitude and daytime equatorial regions are the ionospheric F-region domains least disturbed. This is shown, for example, by Clark and Raitt [1976] in their study of large scale irregularities at altitudes upwards of 400 km. The review by Fejer and Kelley discusses some additional experimental and theoretical results concering mid-latitude irregularities.

At high magnetic latitudes, i.e., $\lambda_m \gtrsim 60^o$, the magnetic field topology provides good electrial coupling to large-scale magnetospheric processes. As a result, ionospheric irregularities can be driven by both localized and remote sources. In general, three sources have been enumerated [Fejer and Kelley, 1980]: particle precipitation, electrostatic turbulence and plasma instabilities. The occurrence of auroras is one of the most obvious ionospheric disturbances at high latitudes, resulting from particle precipitation that is associated with magnetospheric processes. Field-aligned currents, also found in the auroral regions, are apparently the principal source of free energy that leads to electrostatic turbulence and plasma instabilities. A review of theories for high latitude irregularities is provided by Keskinen and Ossakow [1983b]. Ground-based observations of satellite beacon transmissions have very conclusively shown that field-aligned irregularities occur at auroral latitudes [Fremouw et al., 1977; Rino et al., 1978]. The current convective instability has been proposed as the source of the field-aligned irregularities [Ossakow and Chaturvedi, 1979; Chaturvedi and Ossakow, 1979] and numerical simulations have tended to support this theory [Keskinen et al., 1980; Keskinen and Ossakow, 1982]. Experimental observations of F-region density enhancements in the auroral zone consistent with the current convective instability have been reported by Vickrey et al. [1980]. In the lower F-region, both enhancements and depletions of ionization have been found in association with discrete and diffuse auroras [Rodriguez et al., 1981]. Within the polar cap, small scale irregularities can be driven by larger scale density gradients. The larger scale irregularities can arise from velocity shear in the plasma convection or from polar cap precipitation [Weber and Buchau, 1981]. The effect of E-region conductivity on the small scale F-region irregularities and their evolution during convection has been discussed by Vickrey and Kelley [1982] and Kelley et al. [1982a]. Thus, ionospheric irregularities at high magnetic latitudes are associated with magnetosphere-ionosphere coupling processes.

B. A Preview of the Present Study

In this report, we shall discuss recent satellite observations of F-region irregularities at magnetic latitudes $\lambda_m \gtrsim 60^o$, and in the altitude range 170-200 km, i.e., in the high latitude, lower F-region. The objective of this study is to provide a synoptic view of irregularity structure and scale sizes associated with the morphology of the high latitude irregularities. The source regions that we consider are the auroral oval, the polar cusp and the polar cap. We also consider the large scale convection pattern and associated density gradients as a possible source of density fluctuations.

We shall consider only relatively quiet to moderately disturbed conditions, as determined by the Kp and AE indices, in deriving our synoptic view of density irregularities. The study is based upon density measurements obtained during 21 high-latitude passes of the satellite S3-4. The passes were carefully selected to correspond to a moderate level of geomagnetic activity, $K_p \lesssim 2$-3. Since the Kp index is a three-hour average, the better time-resolved index AE was also consulted [Kamei and Maeda, 1981]. All data time intervals discussed in this report correspond to AE indices less than about 500, and are not associated with any strong substorm activity. The AE index for most of the times discussed was on the order of 100. Generally, for this level of activity, the global patterns for particle precipitation, field-aligned currents, and plasma convection at high latitudes are well-defined. For example, electric field measurements have been used by Heppner [1977] to model the large scale plasma motion with a skewed two-cell convection pattern. Heelis et al. [1982] have provided a similar model. The data were also selected to correspond only to the northern polar region, and in all cases except one, for interplanetary magnetic field orientations such that the y-component in solar ecliptic coordinates was negative. Under these conditions the best determined high latitude plasma convection pattern appears to be that of Heppner [1977] in his Figure 6(d). We have adopted that convection pattern as corresponding to the period of our measurements, March to September, 1978. The global pattern of auroral precipitation is represented in our study by the auroral oval model of Holzworth and Meng [1975] and Meng et al. [1977]. They provide the poleward and equatorial boundaries for the occurrence of discrete auroral arcs for various levels of the geomagnetic activity index Q. We adopt their model for Q=2. The pattern of field-aligned currents is generally correlated with the auroras, with upward flowing currents associated with discrete aurora and downward flowing currents associated with diffuse aurora [Potemra et al., 1979]. For the geomagnetic conditions of this study, we shall assume that the global pattern of field-aligned currents is essentially the same as the Q=2 auroral oval, with the possible extension of the equatorial boundary a few degrees further equatorward to include downward flowing currents (i.e., diffuse auroras).

The results of the study show that in general the large scale (> 7.5 km) morphology of density irregularities correlates well with the auroral oval, thus suggesting that particle precipitation and/or current-driven plasma instabilities are the main source of the irregularities. Density fluctuations in the cusp are especially evident, presumably indicating that the soft particle precipitation there is the prime source for irregularites. In the polar cap region the global convection pattern appears to have only a small influence on the transport of large scale size irregularites; there is generally also a marked absence of small scale irregularities.

II. THE S3-4 SATELLITE DENSITY MEASUREMENTS

A. Density Probes

The S3-4 satellite was launched into a polar, sun-synchronous orbit on March 16, 1978 with orbit apogee and perigee at 260 km and 160 km, respectively. The satellite carried a pair of pulsed plasma probes (P^3) supplied by the Naval Research Laboratory. The P^3 instrument was a Langmuir-type probe using a pulse-modulated sweep voltage to generate current-voltage characteristics from which the local electron density, temperature, and plasma potential can be derived. The relative plasma density was measured with two data rates, 100 samples s^{-1} and 800 samples s^{-1}. The maximum resolutions for irregularity scale sizes at the two data rates are $L \sim v_{sc}\ \Delta t \sim 10$ m at the high rate, where $\Delta t = 0.0012$ s and $v_{sc} \sim 7.5$ km s^{-1} is the spacecraft velocity and $L \sim v_{sc}\ \Delta t \sim 75$ m at the low rate, where $\Delta t = 0.01$s. A more complete description along with a discussion of additional analyses possible with the P^3 instrumentation is provided by Szuszczewicz et al. [1982] and references therein.

B. Data Averaging

In this report, only the low data rate measurements are analyzed, and these are averaged to obtain approximately 1-s averages. Plots based on these averages thus contain information on scale sizes $L \gtrsim 7.5$ km; however, diagnostic information on scale sizes down to 75 m is retained. An example of the 1-s average data at high northern latitudes is shown in Figure 1. Approximately ten minutes of data from S3-4 orbit 244 are plotted as a function of universal time (UT), magnetic latitude (MLAT),

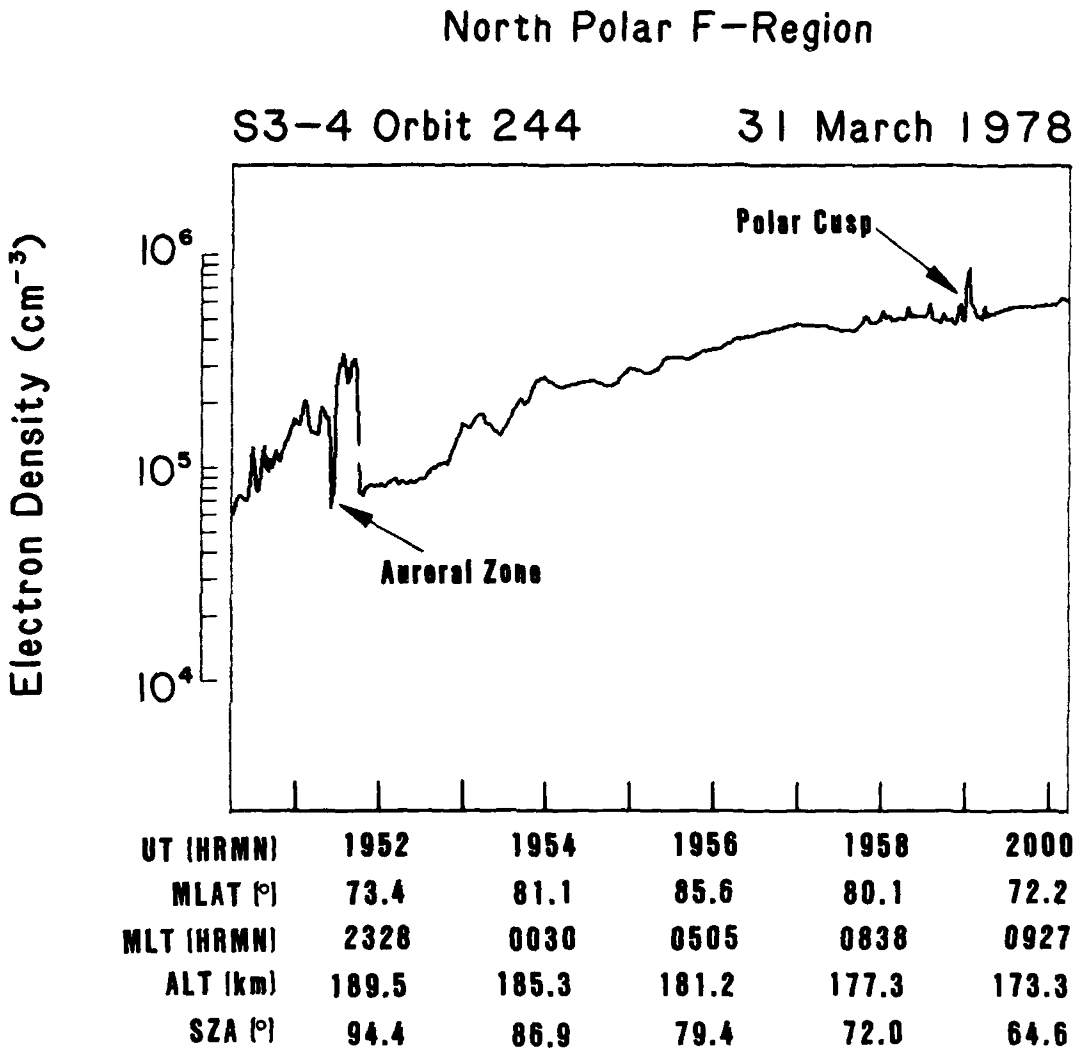

Figure 1. Total density measured during the orbit 244 traversal of northern high latitudes. The polar cusp and auroral zone are identified by the indicated density enhancements.

magnetic local time (MLT), altitude (ALT) and solar zenith angle (SZA). The data plot shows the variation in electron density as the spacecraft traversed north polar magnetic latitudes from about $\lambda_m \sim 60^\circ$ on the anti-sunward side to about $\lambda_m \sim 70^\circ$ on the sunward side. The highest magnetic latitude reached on this pass was about $\lambda_m \sim 86^\circ$, near the center of the data plot. Two regions of distinctive density enhancements are noted on the plot, the auroral zone and the polar cusp. The identities of these regions is supported by analysis considered below. The peak enhancement in the auroral zone is about 3.5×10^5 cm^{-3} while in the cusp, the enhancement reaches 8.0×10^5 cm^{-3}. A smoother but still irregular variation of density is evident in the polar cap region in the central portion of the plot.

C. <u>Solar EUV Ionization</u>

Also evident in Figure 1 is a general density increase from left to right which is due to solar EUV photoionization. This variation is a function of the solar zenith angle and is not directly related to the variations associated with geophysical phenomena, such as precipitating particles or plasma instabilities. In this analysis we wish to remove the solar-dependent ionization component, and we do this by modeling the variation with an alpha Chapman ionization production function, which has the solar zenith angle and the reduced scale height as independent parameters [Rishbeth and Garriott, 1969]. The solar zenith angle variation is already determined by the data because the satellite was in a sun-synchronous orbit so we simply have to adjust the scale height variation to produce the best fit to the data. The best fit is determined graphically using data obtained during a geomagnetically very quiet high latitude pass occurring close to the summer solstice, when the entire northern polar cap was illuminated by sunlight. Since the S3-4 measurements at northern latitudes occurred during northern hemisphere spring and summer, all of the north polar F-region data discussed in this report will refer to ionization characteristics determined after removing the solar-dependent ionization. In this way only effects associated with geophysical disturbances are considered to remain in the data.

D. Geophysically-Related Ionization

The data of orbit 244 in Figure 1 are replotted in Figure 2 with the alpha Chapman function determined for this pass superimposed as the thinner smooth line. The difference between the two curves, $N_e - N_{es}$, is shown in the central panel of Figure 3 where N_e is the total density measured and N_{es} is the modelled solar-dependent ionization component. The density variation now consists of enhancements and depletions relative to the reference density variation given by N_{es}. Thus, the auroral zone contains strong density enhancements above the level that would occur if sunlight were the only source of ionization, while the polar cusp region contains both enhancements and depletions about the level determined by solar photoionization.

In addition to the 1-s average densities plotted in Figure 3, two other diagnostic parameters are shown in the figure. In the lower panel there is a plot of the RMS density fluctuation $\Delta N_{e,rms}$ determined from the data points used in the 1-s averages

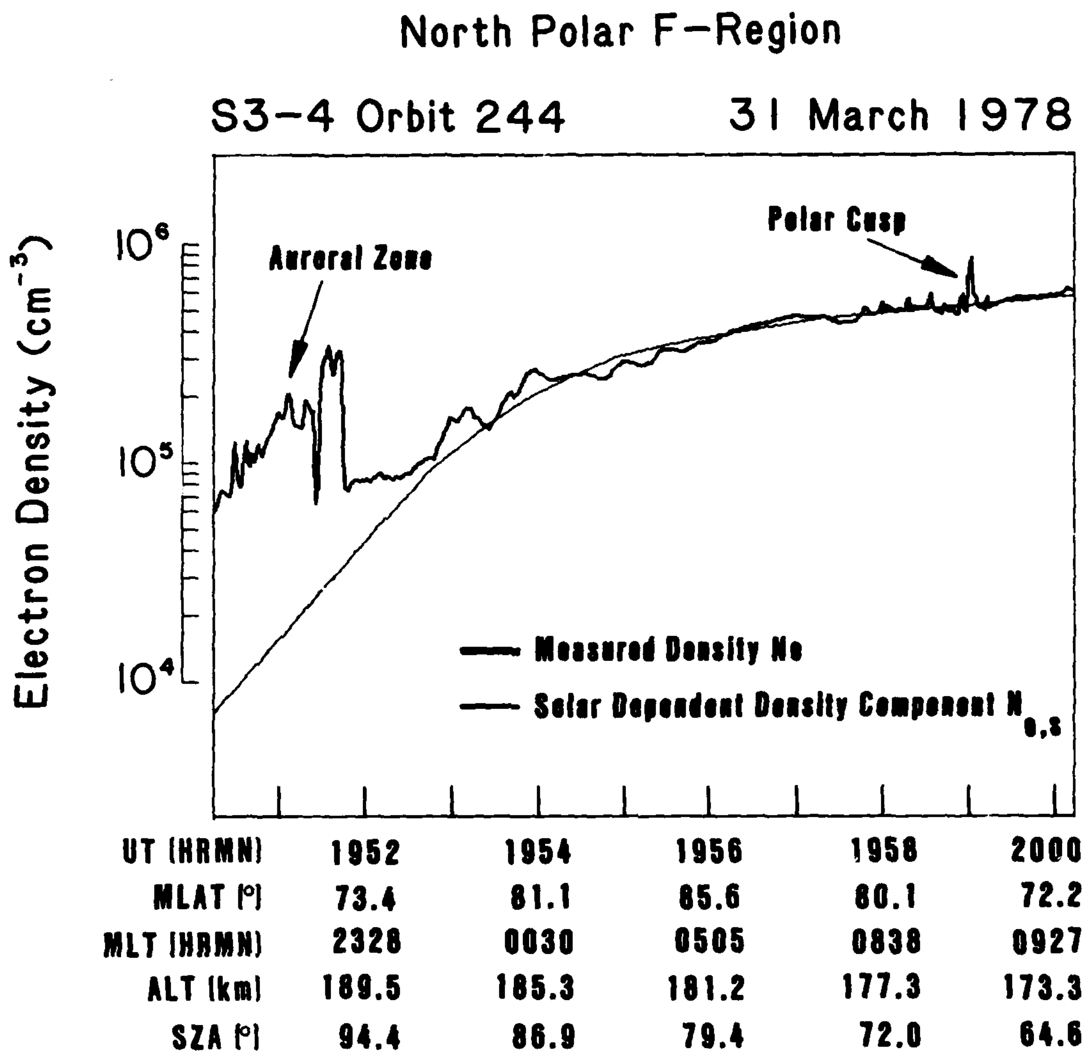

Figure 2. Total density measured on orbit 244, with the modelled Chapman function for solar photoionization superimposed.

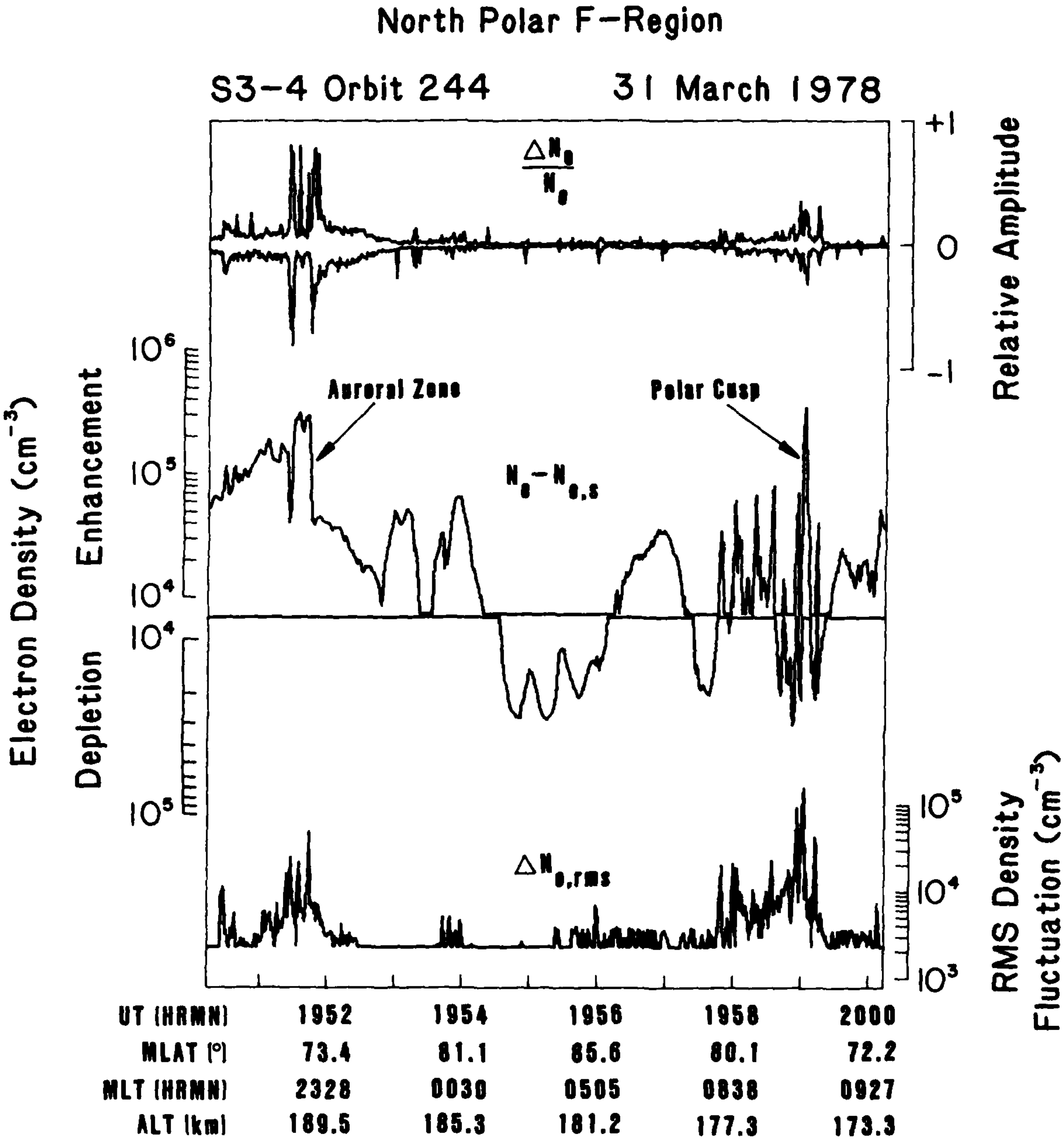

Figure 3. Total density after subtraction of the solar photoionization, $N_e - N_{es}$, thereby containing only geophysically-related variations of density (central panel). The total density curve is based upon 1-s averaged data and thus exhibits variations down to a minimum scale size of 7.5 km. The upper panel is the envelope of minimum and maximum relative fluctuation amplitudes. The lower curve is the RMS fluctuation amplitude for the scale sizes between 7.5 km and 75 m.

of the central panel. The RMS density thus contains information about the fluctuation power for scale sizes 7.5 km > L > 75 m. As indicated in Figure 3, the polar cusp and auroral zones are shown to be a region of enhanced RMS density fluctuations. The polar cap region on the other hand shows a relative absence of RMS density fluctuations in the presence of larger scale (~ 300 km) relative enhancements and depletions. The upper panel of Figure 3 shows a plot of the peak relative amplitude $\Delta N_e/N_e$, where both the maximum and minimum ΔN_e based upon the values used in the 1-s average are determined and divided by the average value. This ratio is constrained to always remain in the range ±1 by a weighting function similar to a tangent function in the range ±π/2. Erroneous data tends to produce relative amplitudes greatly exceeding ±1; erroneous points are given the extremum values and are thus identified. Non-erroneous data can only approach asymtotically close to ±1. In general, the relative amplitudes are not distorted significantly by the weighting function until they reach values greater than about |± 0.9|. As shown in Figure 3, the relative amplitudes $\Delta N_e/N_e$ indicate large relative fluctuations in density in the auroral zone. The absolute values of these relative amplitudes are seen to maximize at the large density gradients in the auroral zone. The polar cusp is characterized by somewhat smaller values of peak relative density amplitudes.

The data of Figure 3 illustrates the basic data analysis approach of this study: the determination of 1-s averages of the electron density with the solar ionization removed, with the additional diagnostics of RMS density fluctuations and peak relative amplitudes. An examination of these F-region irregularity characteristics with respect to the location of the auroral zone, polar cap, and polar cusp can therefore reveal the general morphology of high latitude irregularities for scale sizes down to $L \sim 75$ m.

E. High Latitude Coverage

The sun synchronous orbit of S3-4 produced orbit trajectories generally aligned with the 1030-2230 local time meridian in geodetic coordinates. However, due to the daily motion of the magnetic pole in a circle of radius $\sim 11^{\circ}$ about the geodetic pole, the coverage of S3-4 extended over a polar region including 1000-1200 MLT on the sunward side and 2100-2300 MLT on the anti-sunward side. The high latitude trajectories of orbits 244 and 1698, shown in the polar plot of Figure 4, essentially indicate the dawnward and duskward limits of S3-4 coverage in geomagnetic coordinates. The dots on the trajectories indicate one-minute intervals, and the arrowhead shows the direction of spacecraft motion. Several UT values are indicated, corresponding to data plots in other figures. The auroral oval shown is the model of Holzworth and Meng [1975] which is based upon DMSP photographs that show discrete auroras encircling or nearly encircling the magnetic pole. The oval boundaries are essentially circles offset from the magnetic pole by varying amounts depending on the value of the magnetic activity index Q. The Q=2 auroral oval corresponds to moderately quiet conditions and serves as a reference for the S3-4 data obtained for $K_p \lesssim 2\text{-}3$.

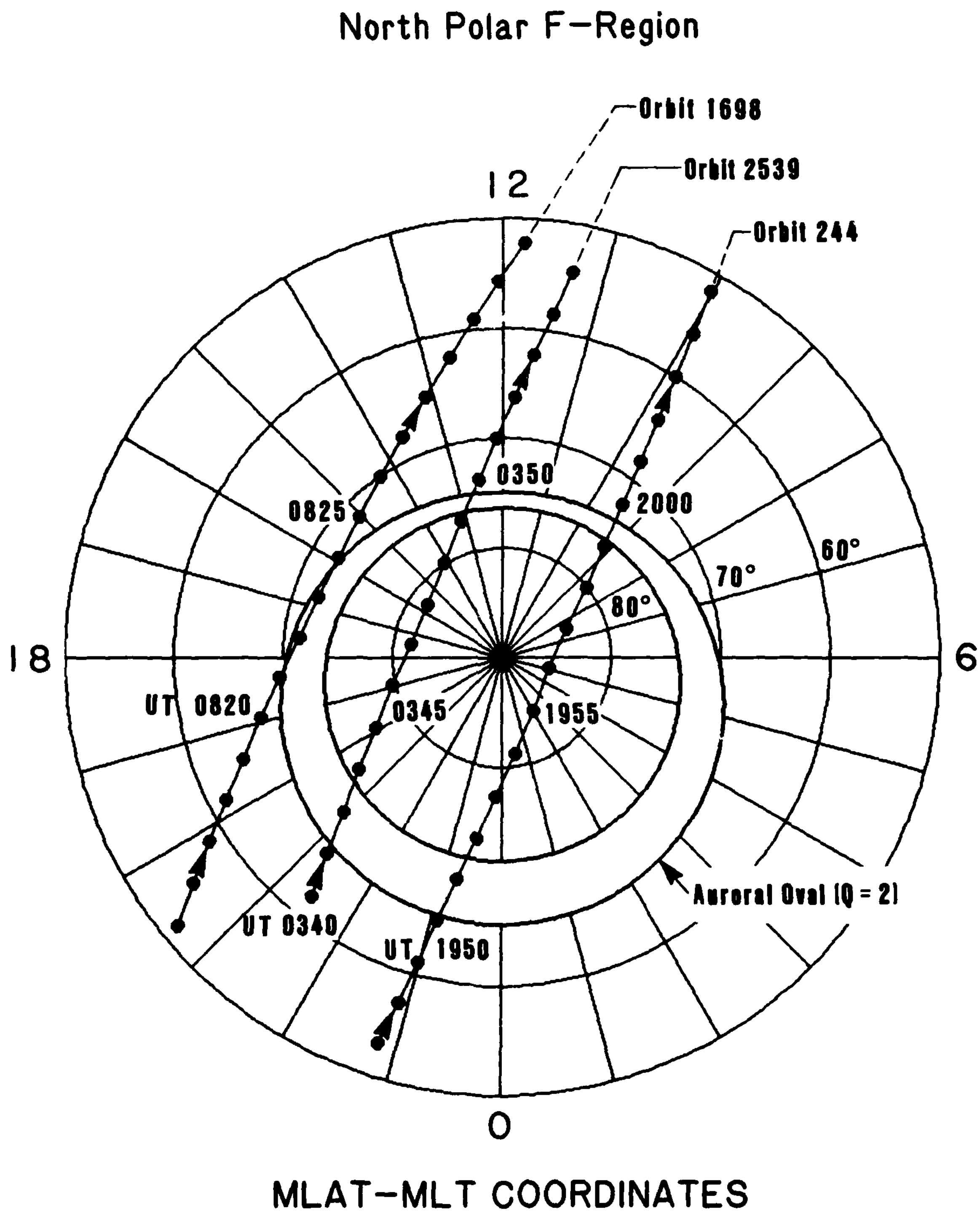

Figure 4. Polar plot of northern high latitudes showing the transpolar trajectories of orbits 244, 1698, and 2539. The black dots on the trajectories are one minute apart in UT. The model auroral oval for Q=2 is included as a reference.

The orbit 244 trajectory on Figure 4 indicates that between about 1951 UT and 1953 UT the auroral oval is encountered. Referring to the data plot of Figure 3 shows that the region of enhanced densities, RMS fluctuations, and peak relative density fluctuations identified with the auroral zone occurs in the same UT interval. Likewise, the location of the polar cusp in Figure 3 at about 1959 UT corresponds with the cusp location at the poleward edge of the auroral oval in Figure 4. The large scale relative depletion centered at about 1955 UT in Figure 3 is located well inside the auroral oval of Figure 4 very near the region where polar cap ionospheric depletions or "holes" have been reported [Brinton et al., 1978]. Thus, there is an apparent good correspondence between the large scale geomagnetic morphology implied by the auroral oval model of Figure 4 and the occurrence of distinct density irregularities as shown by the S3-4 data of Figure 3.

The trajectory for orbit 1698 in Figure 4 suggests that the auroral oval is encountered on the duskward side between about 0821 UT and 0824 UT. The data plot for orbit 1698 is shown in Figure 5 in a format similar to Figure 2, with the measured density indicated by the heavy trace superimposed on the fitted solar-dependent density component.

A relative density *enhancement* is detected between about 0821 UT and 0825 UT, which is thus identified with the auroral zone. The long period of time, about 3 minutes, that the spacecraft remains within the auroral zone is clearly due to the orbit trajectory being nearly parallel to the auroral oval

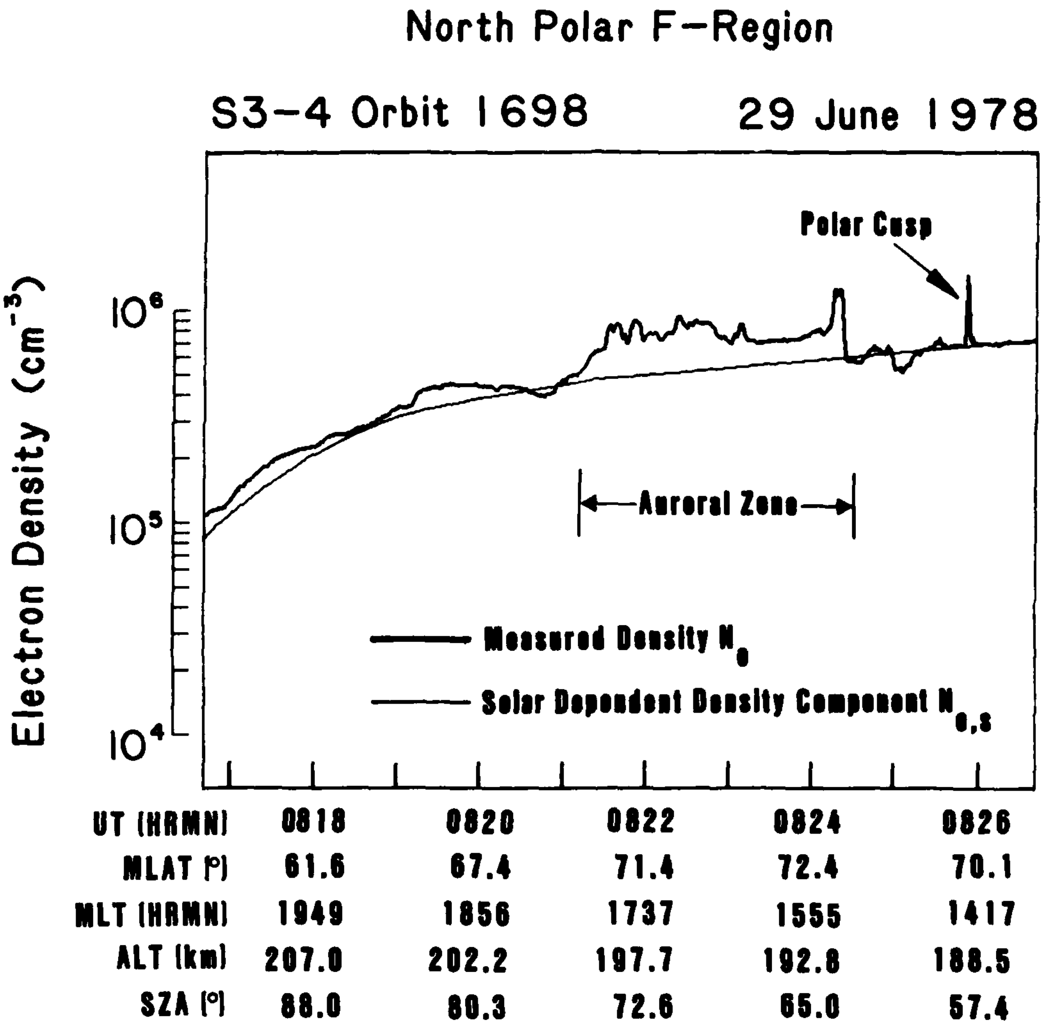

Figure 5. Total density measured during the orbit 1698 traversal of the northern high latitudes, with the modelled solar photoionization indicated.

boundaries. At earlier times, corresponding to magnetic latitudes $\lambda_m \sim 60^\circ-68^\circ$, relative density enhancements are also evident. These enhancements may possibly be associated with the diffuse auroras which generally extend to lower latitudes than the discrete auroras upon which the auroral oval model of Figure 4 is based. The sharp density enhancement with narrow latitudinal width at about 0826 UT is identified as the polar cusp. Referring to Figure 4 suggests that at 0826 UT, when the magnetic latitude $\lambda_m \sim 70^\circ$, the spacecraft would be past the polar cusp. We believe this apparent inconsistency arises only because the boundaries of the oval model are statistically determined. Discrete aurora can certainly occur at lower latitudes, such that the poleward boundary of the auroral oval moves to about $\lambda_m \sim 70^\circ$. Cusp locations based upon soft particle precipitation [Meng, 1983] have often been found at the location suggested by S3-4 data. In Figure 6 the density data is shown in the format of Figure 3. The auroral zone now appears as a well-defined density enhancement correlated with an increased level of RMS density fluctuations. Relative fluctuations $\Delta N_e/N_e$ in the auroral zone are very small, suggesting that large density gradients are absent at scale sizes above 75 m. With $K_p \sim 2$, geomagnetic conditions were relatively quiet during orbit 1698. However, in the cusp region, narrow latitudinal structures are observed with the RMS density fluctuation level reaching large values $\sim 10^5$ cm^{-3} and relative amplitudes $\sim \pm 0.3$. The cusp characteristics in terms of density, RMS fluctuations, and relative amplitudes are very similar to the case in orbit 244.

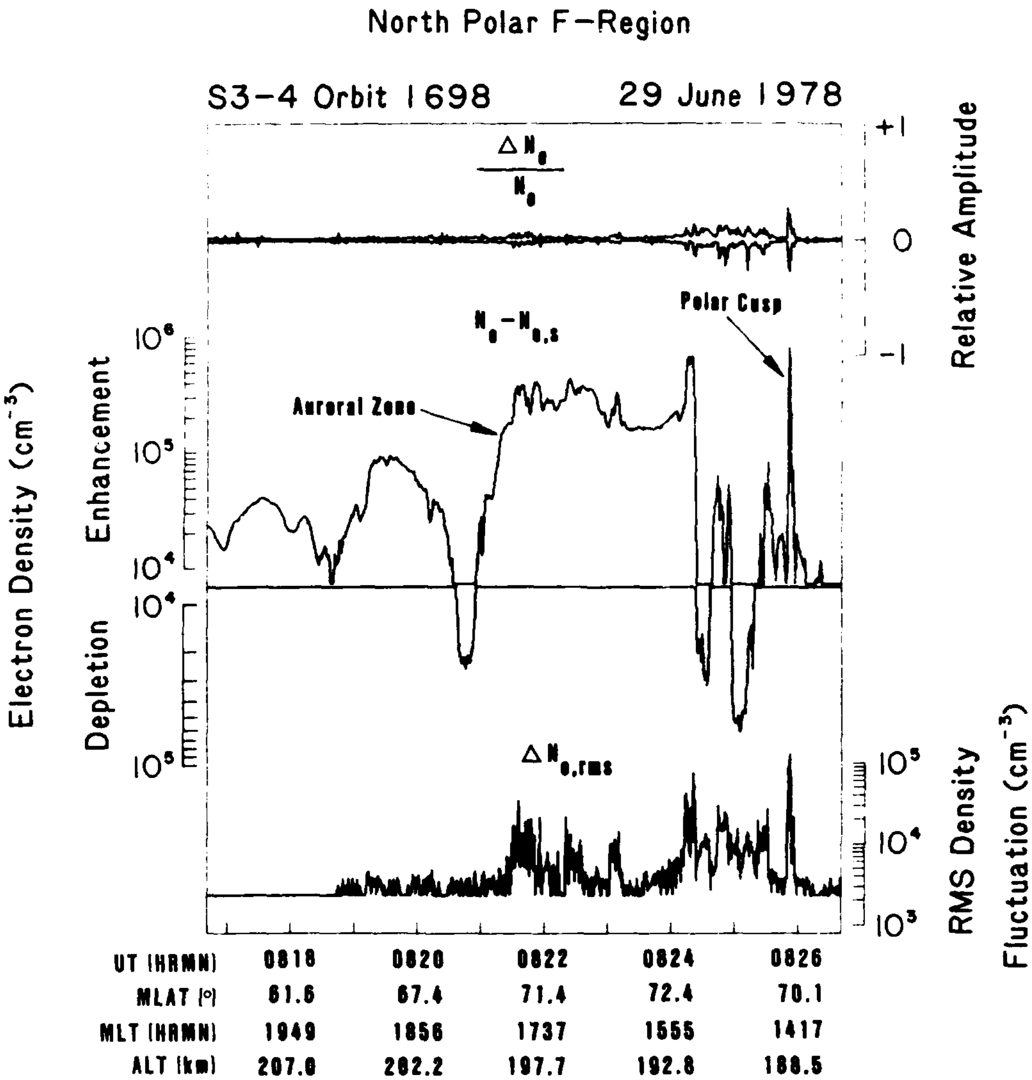

Figure 6. The orbit 1698 plot of geophysically-related density variations, in a format similar to Figure 3.

As a final example of specific irregularity observations, we examine orbit 2539 which had a trajectory passing approximately through the center of the region of S3-4 high latitude coverage. The K_p during this pass was about 1, quiet in terms of geomagnetic disturbances. Orbit 2539 is also of particular interest because, as Figure 4 illustrates, the trajectory passes through 1230 MLT and $\lambda_m \sim 75^o$, near the most commonly detected location of the polar cusp. The measured density profile on orbit 2539 is presented in Figure 7. Density enhancements associated with the polar cusp clearly stand out at 0350 UT. The structure of the density enhancements suggests a fairly sharp onset of fluctuations at the equatorward boundary with a gradual decrease in fluctuations in the poleward direction. Larger scale but less intense density enhancements are detected near 0345 UT and 0346 UT, which occur well within the polar cap. In Figure 8 we present the orbit 2539 data after removing the solar-dependent ionization component. Several features of the cusp are apparent. Although individual density enhancements retain the narrow latitudinal widths previously observed, the region of cusp-associated enhancements is wider than previously observed, on the order of 450 km. The low latitude boundary of the cusp suggests that a finite transition region occurs there rather than a sharp boundary. The RMS density fluctuations exceed 10^5 cm^{-3} and clearly show that the cusp contains a substantial level of small scale fluctuations, while the relative amplitudes $\Delta N_e/N_e$ again indicate that density gradients peak in the cusp. Poleward of the cusp, both relative enhancements and depletions occur with

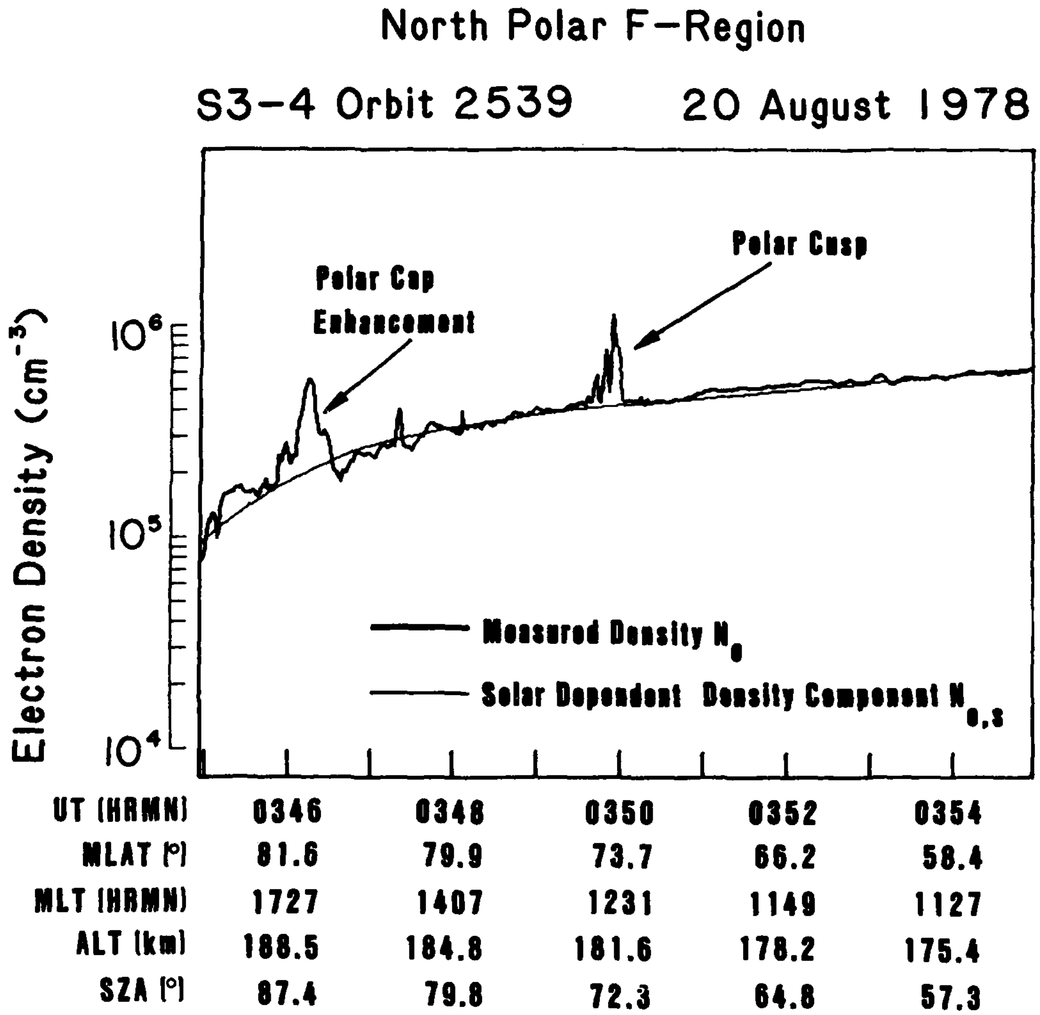

Figure 7. Total density measured during the orbit 2539 traversal of northern high latitudes, with the modelled solar photoionization. The polar cusp encounter shows a substantial density enhancement above the solar photoionization backgound. The polar cap density enhancement is of an intensity comparable to auroral zone enhancements.

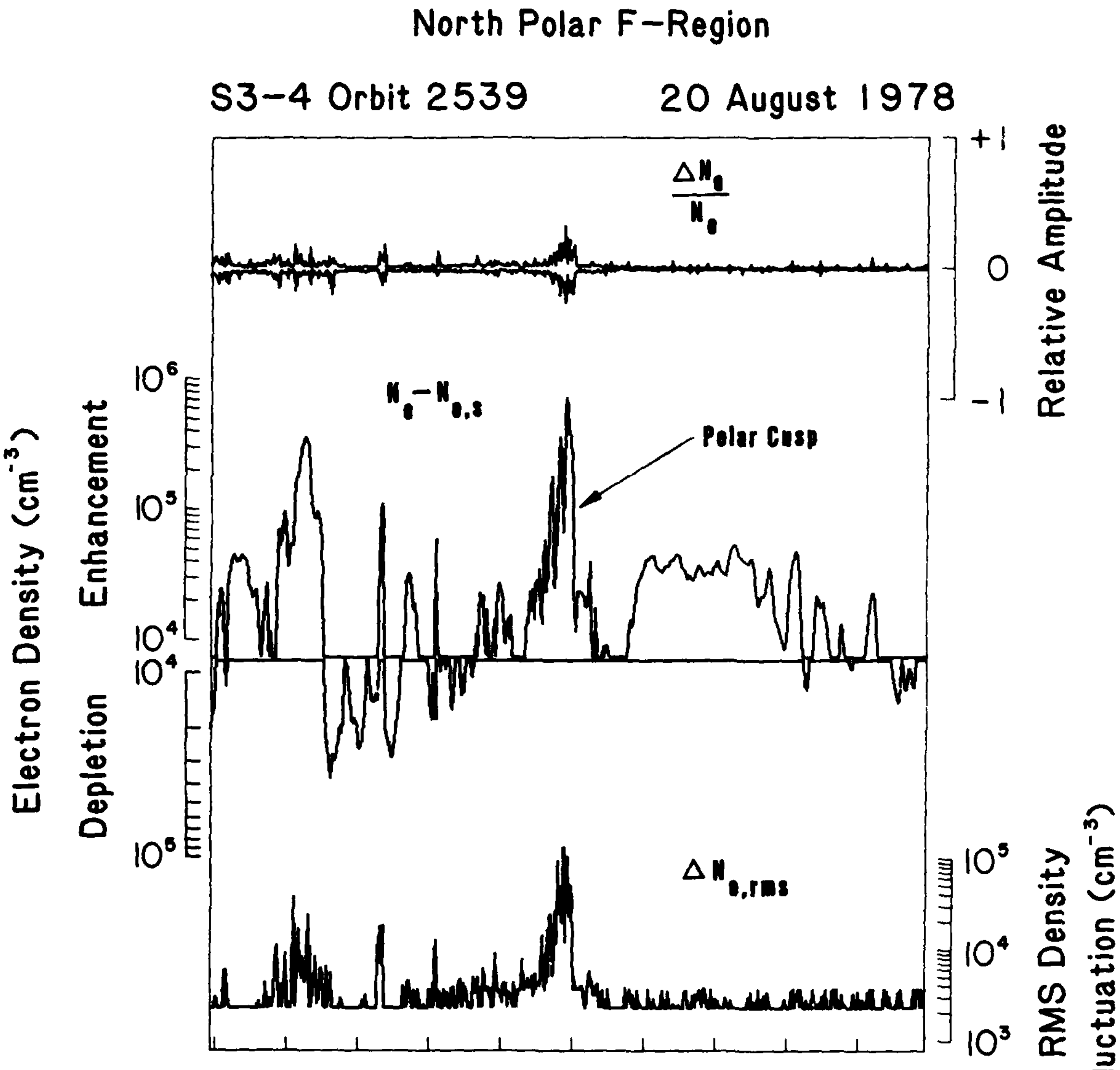

UT (HRMN)	0346	0348	0350	0352	0354
MLAT (°)	81.6	79.9	73.7	66.2	58.4
MLT (HRMN)	1727	1407	1231	1149	1127
ALT (km)	188.5	184.8	181.6	178.2	175.4

Figure 8. The orbit 2539 plot of geopnysically-related density variations, in a format similar to Figures 3 and 6.

small variable levels of small scale fluctuations and density gradients. The enhancement, centered at about 0346 UT has an increased RMS density fluctuation level, similar to auroral zone fluctuations. However, referring to Figure 4 shows that at 0346 UT the spacecraft was near $\lambda_m \sim 80^{\circ}$ and thus well inside the polar cap region. We suggest that the enhancement at 0346 UT may therefore be associated with a polar cap auroral arc, possibly sun-aligned arcs [Ismail et al., 1977; Meng, 1981] or perhaps the center bar of the theta aurora discussed by Frank et al., [1982]. Equatorward of the low latitude cusp boundary, distinct density enhancements are also obvious. These enhancements appear to have very little small scale structure as indicated by the low level of RMS fluctuations and relative amplitudes.

III. Synoptic Study

A. Geophysical Morphology

In the preceeding discussion we have shown specific examples of density irregularities associated with the auroral oval pattern for quiet to moderately disturbed conditions. In this study, the auroral oval is assumed to represent the geophysical morphology for particle precipitation and field-aligned currents, both of which can lead to the density irregularities observed. The correlation between density enhancements and the statistically-favored locations of auroral arcs and the polar cusp has been very good, in general.

Another possible source for density irregularities is associated with polar cap plasma convection since density gradients that might develop during convection can, in principal, drive plasma instabilities. Generally, the two-cell convection pattern is skewed in different directions according to the orientation of the interplanetary magnetic field (IMF) that connects to the magnetosphere. For the S3-4 measurements we have selected all high latitude passes, except one, to correspond to the IMF y-component in solar ecliptic coordinates, to be negative, i.e., to correspond to "away" sector structures in the solar wind. We have adopted the figure of equipotential contours determined by Heppner [1977] for IMF B_y negative to represent the high latitude convection pattern, as shown in Figure 9. A comparison of Figures 4 and 9 shows that the Q = 2 auroral oval is well-correlated with the large scale features of the convection pattern. Thus, the sunward portion of the auroral oval lies exactly where the velocity convection streamlines reverse direction from sunward to anti-sunward, and the two smallest convection cells shown are centered near the high latitude boundary of the auroral oval. The polar cap region, inside the auroral oval, is entirely in the region of anti-sunward convection. Figures 4 and 9 thus represent the underlying geophysical morphology to which our measurements of density irregularities will be referred.

B. Irregularity Morphology

The general morphology of F-region density irregularities for the 1-s average measurements is shown by the gray-shaded representation in Figure 10. The gray scale at the bottom of the figure is used to convert a given density value to some shade of gray. The gray scale is divided into ten levels of increasing

North Polar Convection Streamlines

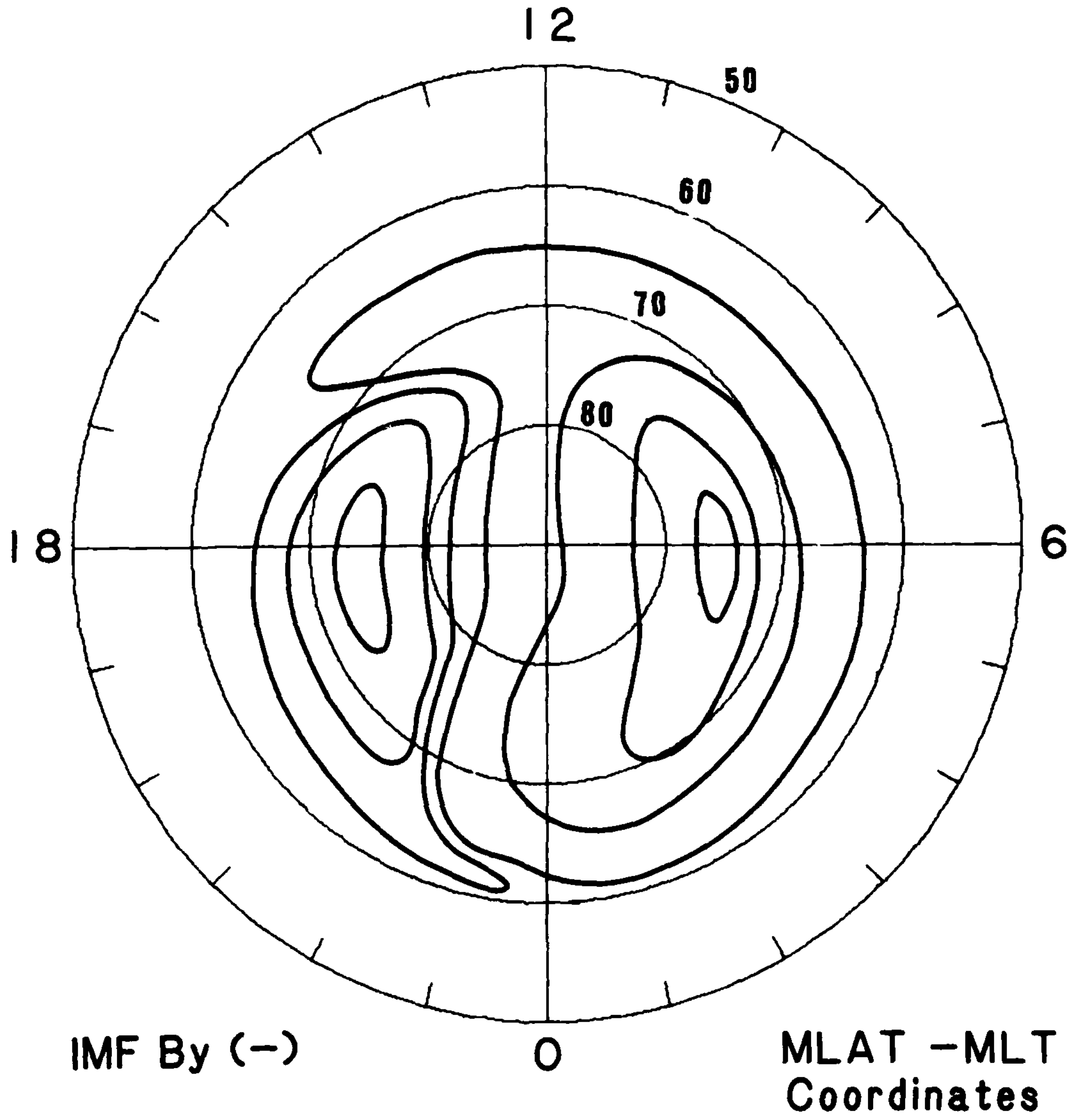

Figure 9. High latitude convection pattern for the interplanetary magnetic field B_y component negative. The streamlines are based upon the electric field equipotential contours of Heppner [1977].

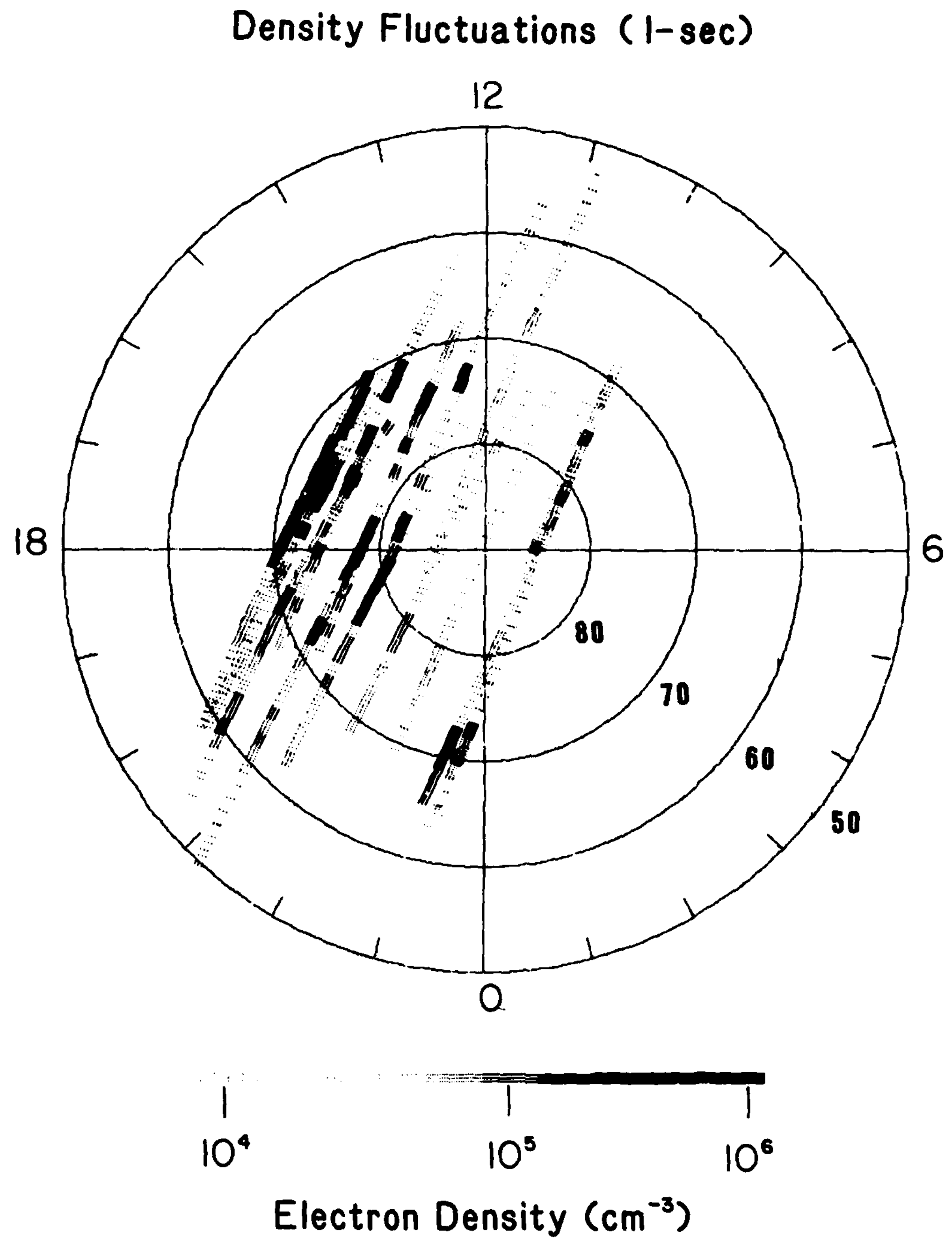

Figure 10. A gray-shaded polar plot (magnetic latitude-magnetic local time coordinates) of 1-s averaged density fluctuations showing the distribution of irregularity scale sizes ≥ 7.5 km. The auroral oval and polar cusp exhibit the most intense density fluctuations. Refer to Figure 4 for the auroral oval model.

darkness, corresponding to ten equal logarithmic increments of electron density. Thus, the scale ranges from white for N_e < $10^4 cm^{-3}$ to black for $N_e \geq 6.31 \times 10^5 cm^{-3}$. Each gray-shaded element (analogous to a pixel in imaging systems) in the plot is a square of spatial dimensions 150 km x 150 km. The 150-km dimension parallel to the orbit trajectory corresponds to 20 s of time at a spacecraft velocity of 7.5 km s^{-1}. The 150-km dimension perpendicular to the orbit trajectory is arbitrary, chosen simply to give the pixel a finite size. The pixels are plotted along the corresponding orbit trajectory in geomagnetic coordinates. The white regions between orbit trajectories are spatial regions not sampled by the spacecraft. The data interval on each orbit is typically ten minutes long; therefore with a spacecraft velocity of 7.5 km s^{-1}, about 30 pixels of gray shading occur for each data interval. From the twenty-one data intervals selected, we can thus construct a 600-pixel "image" of the density irregularities. A given pixel increment along the spacecraft trajectory corresponds to twenty 1-s average values of density. From each group of twenty we have picked the maximum value of the 1-s averages to convert to the gray-scale used for plotting Figure 10. Thus, the plot shows the measured high latitude distribution of density irregularities for scale sizes L $\geq$ 7.5 km. A comparison of Figure 10 with Figure 4 illustrates the relationship of the irregularity distribution with the auroral oval model. The duskward side of the oval appears to correlate well with the enhanced density values as indicated by the darker shades in Figure 10. Individual black pixels on the sunward size correspond to the polar cusp observations of strong density enhancements. The smoothing effect of the pixel size obscures some of the cusp enhancements, however, every cusp encounter in the data sample has been verified with detailed plots such as Figures 3, 6 and 8. Evidence of polar cap density enhancements are also present in Figure 10, especially near $\lambda_m \sim 80^\circ$ and 1800 MLT. If we take averages of the twenty values of density within each pixel interval we obtain 20-s averages corresponding to scale sizes $L \geq 150$ km for the density irregularities. Figure 11 shows the gray-shaded "image" of these 20-s averages. A comparison of Figures 11 and 10 shows that the 20-s averages ($L \geq 150$ km) have tended to slightly narrow the duskward region correlated with the auroral oval while providing somewhat better definition of the anti-sunward portion of the auroral oval. In addition, irregularities at latitudes equatorward of the auroral oval seem to be more prominent. Some of the cusp signatures, however, have disappeared at the $L \geq 150$ km scale size. The polar cap region appears to be relatively unchanged. It should be noted that the gray scales for Figures 10 and 11 are slightly different from each other, the scales having been adjusted to produce the best contrast for each figure. Thus the comparison done above is one of contrasts and not of particular shades of gray.

As we have previously discussed the 1-s RMS density fluctuations provide a measure of the strength of irregularities with scale sizes 7.5 km > L > 75 m. The cusp and auroral zone were both characterized by having a significant level of RMS density

Density Fluctuations (20-sec)

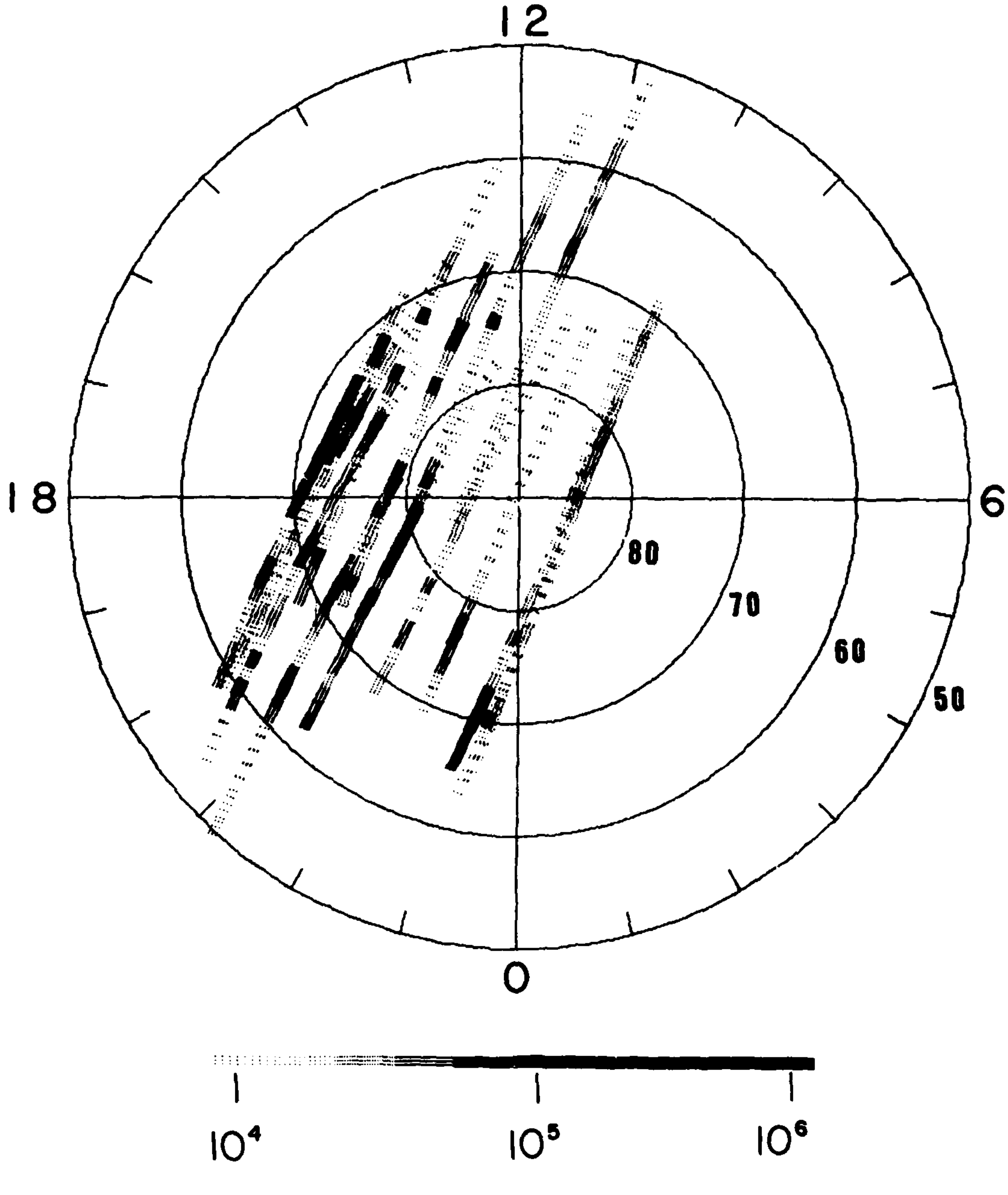

Figure 11. A gray-shaded polar plot, similar to Figure 10, of 20-s averaged density fluctuations. The distribution refers to scale sizes $\geq$ 150 km.

fluctuations as shown in Figures 3, 6 and 8. In Figure 12 we have plotted the 1-s RMS density fluctuations in gray-shaded format. The value for each pixel in Figure 12 is the maximum of the twenty 1-s RMS fluctuation values occurring within each pixel increment. The figure confirms that scale sizes 7.5 km > L > 75 m have their greatest strengths in the polar cusp and auroral oval. We have verified this general result by examining the detailed individual data increments. At various regions within the polar cap, 7.5 km > L > 75 m scale sizes are also evident, however not to the same degree as in the cusp and auroral oval. In Figure 13 we have produced power averages of the twenty RMS fluctuation values within each pixel interval to obtain 20-s RMS density fluctuation values. These values give the RMS fluctuation level for scale sizes 150 km > L > 75 m, and thus represent the total power for a wide spectrum of irregularities. In this figure the cusp enhancements stand out again, however the auroral oval and polar cap are much less distinguishable from each other.

IV. Summary and Conclusions

Our study of high-latitude F-region irregularities has shown that for moderate geomagnetic activity conditions ($K_p \lesssim$ 2-3), enhanced density fluctuations with scale sizes 150 km > L > 75 m are associated with the polar cusp and auroral oval in the altitude range 170-200 km. The density irregularities are presumably a direct effect of particle precipitation in the cusp and auroral zone. On individual orbital passes through the sunlit high latitude F-region the cusp-associated irregularities are generally more intense than the auroral oval irregularities. Both

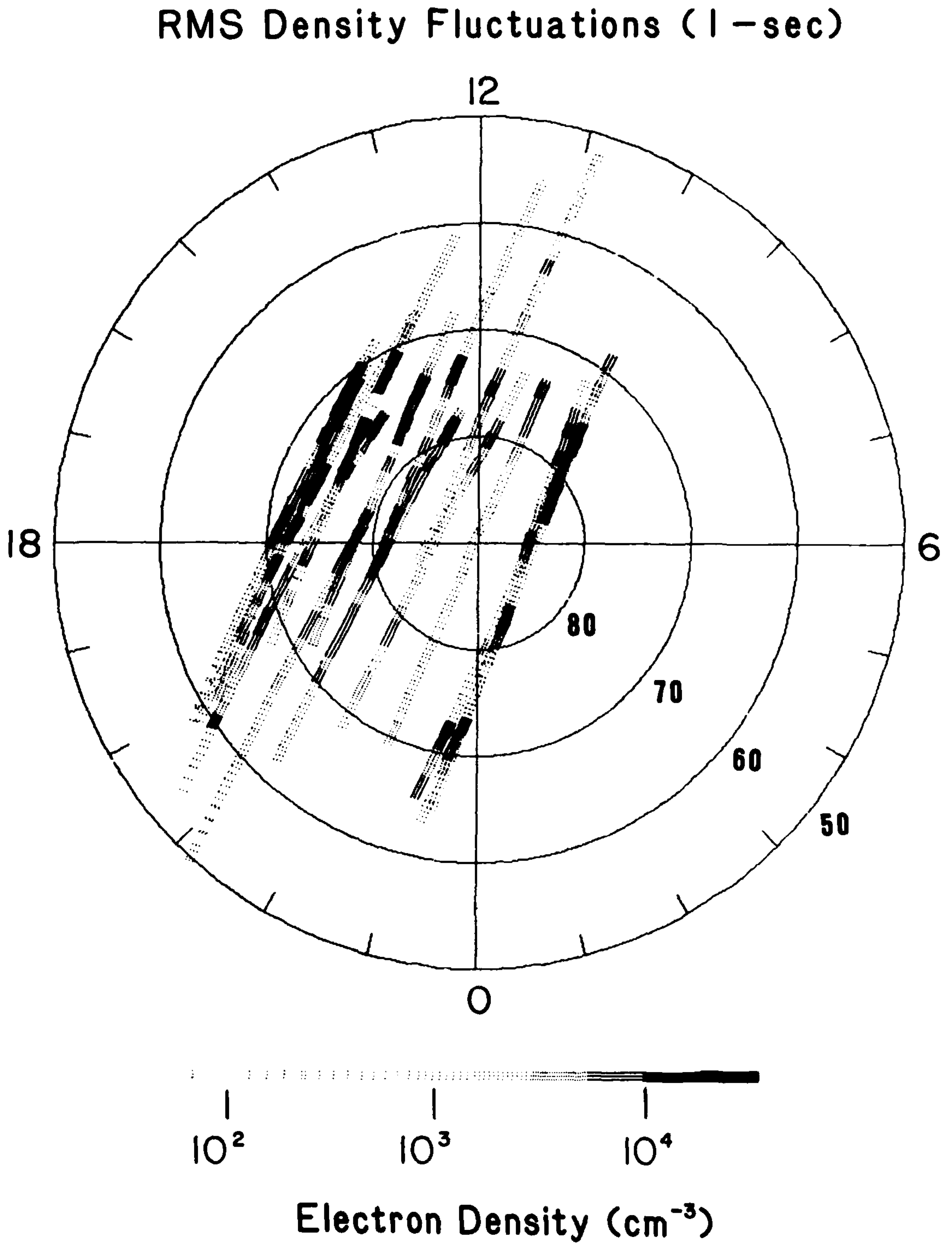

Figure 12. A gray-shaded polar plot of 1-s averaged RMS density fluctuations showing the distribution of irregularity scale sizes between 7.5 km and 75 m.

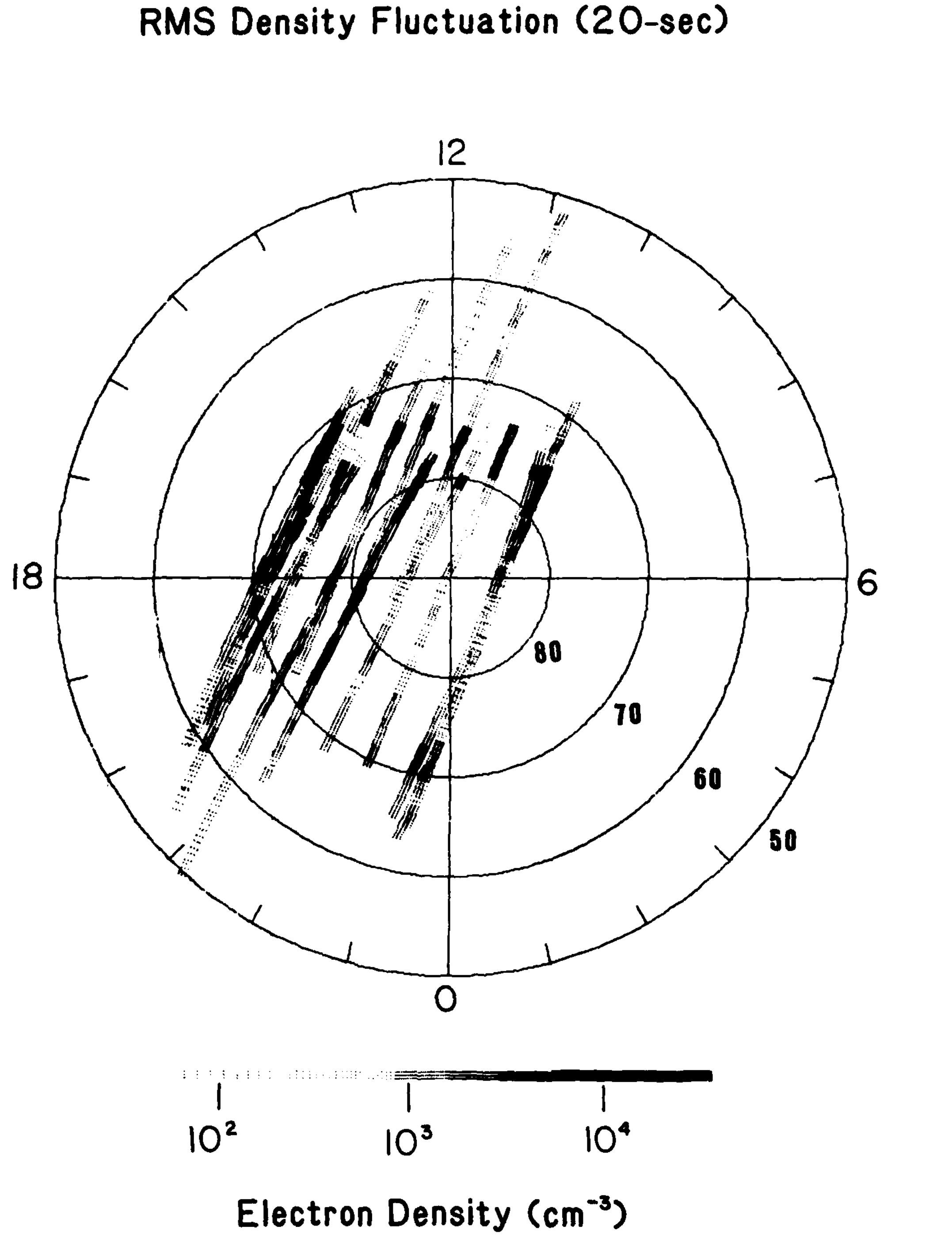

Figure 13. A gray-shaded polar plot of 20-s averaged RMS density fluctuations showing the distribution of irregularity scale sizes between 150 km and 75 m.

irregularity regions, however, are substantial perturbations on the background photoionization. In the cusp region the maximum density enhancements are observed to reach absolute densities comparable to the F-region maximum due to photoionization in the noontime equatorial region, i.e., about 10^6 cm^{-3} while in the auroral zone the maximum absolute density enhancements reach about 8×10^5 cm^{-3}. Our study thus suggests that in the lower F-region the precipitation associated with the polar cusp is more effective in producing density enhancements than auroral precipitation. This result appears to be at variance with calculations by Roble and Rees [1977] which indicate that cusp soft particle precipitation under sunlit conditions has little effect on the background photoionization below about 300 km altitude.

Small scale (7.5 km >L> 75 m) density irregularities, are found to be associated principally with the cusp and auroral zones, there being a marked absence of these fluctuations within the polar cap. These smaller scale irregularities are associated with large scale ($L \gtrsim 7.5$ km) irregularities that occur in regions of expected particle precipitation. Recent reports [Kelley et al., 1982a; Keskinen and Ossakow, 1983a] suggest that the small scale structure can result from the $\bar{E} \times \bar{B}$ gradient drift instability through a cascading from large scale irregularities associated with structured particle precipitation. Thus, the absence of structured particle precipitation in the polar cap would explain the absence of small scale irregularities therein. Kelley et al., show that an enhanced E-region conductivity, such as would occur under the sunlit conditions of the present study, enhances the cross-field diffusion rate and therefore tends to limit the lifetime of small scale irregularities. Irregularity decay rates due to chemical recombination and diffusion are expected to be equal at about 300 km altitude [Jones and Rees, 1973] with recombination rates dominant at lower altitudes. Thus, for the altitude range of the present observations (170-200 km) it is possible that polar cap small scale irregularities are primarily removed by recombination even though an enhanced diffusion rate is expected. The relative importance of the two decay modes cannot be determined in the present study.

The overall morphology derived from our observation implies that the large scale convection pattern does not appreciably redistribute high latitude irregularities. When intense polar cap irregularities are observed, for example, particle precipitation is suggested rather than the effects of convection, such as velocity shear. However, a characteristic convection effect, the recombination decay of irregularities with long travel times in regions free of particle precipitation may have been detected in our Figures 10 and 11. The reduced level of irregularities in the region $\lambda_m \sim 80^\circ$ and 0100 MLT of the polar cap corresponds closely to the ionospheric "hole" reported by Brinton et al. [1978]. A relative depletion in the same region is shown by the density plot in Figure 3.

We conclude that at the low altitude of our S3-4 observations the morphology of F-region irregularities is primarily the result of particle precipitation, and that the precipitation produces substantial density enhancements even in the presence of photoionization. The polar cusp in particular is a region of strong density fluctuations, with auroral precipitation, both in the auroral oval and in polar cap arcs producing nearly comparable density enhancements.

ACKNOWLEDGMENT

The authors wish to thank the Air Force Space Test Program, the Naval Space Systems Activity and the Office of Naval Research for support throughout this program. We are also indebted to the Defense Nuclear Agency for continued sponsorship under Program Element 62715H (MIPR 82-684). This work was further supported within the Ionospheric and Stratospheric Task Area (0949-0) and conducted within the Space Plasma Diagnostics Group of the Space Science Division.

REFERENCES

Brinton, H. C., '. M. Grebowsky, and L. H. Brace, The high-latitude winter F region at 300 km: Thermal plasma observations from AE-C, J. Geophys. Res., 83, 4767, 1978.

Chaturvedi, P. K., and S. L. Ossakow, Nonlinear stabilization of the current convective instability in the diffuse aurora, Geophys. Res. Lett., 6, 957, 1979.

Clark, D. H., and W. J. Raitt, the global morphology of irregularities in the topside ionosphere as measured by the total ion current probe on ESRO-4, Planet. Space Sci., 24, 873, 1976.

Fejer, B. G., and M. C. Kelley, Ionospheric irregularities, Rev. Geophys. Space Phys., 18, 401, 1980.

Frank, L. A., J. D. Craven, J. L. Burch, and J. D. Winningham, Polar views of the earth's aurora with Dynamics Explorer, Geophys. Res. Lett., 9, 1001, 1982.

Fremouw, E. J., C. L. Rino, R. C. Livingston, and M. C. Cousins, A persistent subauroral scintillation enhancement observed in Alaska, Geophys. Res. Lett., 4, 539, 1977.

Heelis, R. A., J. K. Lowell, and R. W. Spiro, A model of the high-latitude ionospheric convection pattern, J. Geophys. Res., 87, 6339, 1982.

Heppner, J. P., Empirical models of high-latitude electric fields, J. Geophys. Res., 82, 1115, 1977.

Holzworth, R. H., and C. -I. Meng, Mathematical representation of the auroral oval, Geophys. Res. Lett., 2, 377, 1975.

Ismail, S., D. D. Wallis, and L. L. Cogger, Characteristics of polar cap sun-aligned arcs, J. Geophys. Res., 82, 4741, 1977.

Jones, R. A., and M. H. Rees, Time dependent studies of the aurora-I. Ion density and composition, Planet. Space Sci., 21, 537, 1973.

Kamei, T., and H. Maeda, Auroral electrojet indices, 1978, Data Books Nos. 3 and 4, WDC-C2 for Geomagnetism, Faculty of Science, Kyoto University, 1981.

Kelley, M. C., Equatorial spread F: A review of recent experimental results, in Wave Instabilities in Space Plasmas, edited by P. J. Palmadesso and K. Papadopoulos, D. Reidel Publishing Co., 1979.

Kelley, M. C., J. F. Vickrey, C. W. Carlson, and R. Torbert, On the origin and spatial extent of high-latitude F region irregularities, J. Geophys. Res., 87, 4469, 1982a.

Kelley, M. C., R. C. Livingston, C. L. Rino, and R. T. Tsunoda, The vertical wave number spectrum of topside equatorial spread F: Estimates of backscatter levels and implications for a unified theory, J. Geophys. Res., 87, 5217, 1982b.

Keskinen, M. J., S. L. Ossakow, and B. E. McDonald, Nonlinear evolution of diffuse auroral F region ionospheric irregularities, Geophys. Res. Lett., 7, 573, 1980.

Keskinen, M. J., E. P. Szuszczewicz, S. L. Ossakow, and J. C. Holmes, Nonlinear theory and experimental observations of the local collisional Rayleigh-Taylor instability in a descending equatorial spread F ionosphere, J. Geophys. Res., 86, 5785, 1981.

Keskinen, M. J., and S. L. Ossakow, Nonlinear evolution of plasma enhancements in the auroral ionosphere, 1, Long wavelength irregularities, J. Geophys. Res., 87, 144, 1982.

Keskinen, M. J., and S. L. Ossakow, Nonlinear evolution of convecting plasma enhancements in the auroral ionosphere, 2, Small scale irregularities, J. Geophys. Res., 88, 474, 1983a.

Keskinen, M. J., and S. L. Ossakow, Theories of high latitude ionospheric irregularities: A review, submitted to Radio Science, 1983b.

Meng, C. -I., Auroral arcs observed by DMSP satellites, in Physics of Auroral Arc Formation, edited by S. -I. Akasofu and J. R. Kan, American Geophysical Union, Washington, DC, 1981.

Meng, C. -I., Case studies of the storm time variation of the polar cusp, J. Geophys. Res., 88, 137, 1983.

Meng, C. -I., R. H. Holzworth, and S. -I. Akasofu, Auroral circle - Delineating the poleward boundary of the quiet auroral belt, J. Geophys. Res., 82, 164, 1977.

Ossakow, S. L., A review of recent results on spread F theory, in Wave Instabilities in Space Plasmas, edited by P. J. Palmadesso and K. Papadopoulos, D. Reidel Publishing Co., 1979.

Ossakow, S. L., and P. K. Chaturvedi, Current convective instability in the diffuse aurora, Geophys. Res. Lett., 6, 332, 1979.

Potemra, T. A., T. Iijima, and N. A. Saflekos, Large-scale characteristics of Birkeland currents, in Dynamics of the Magnetosphere, edited by S. -I. Akasofu, D. Reidel, 1979.

Rino, C. L., R. C. Livingston, and S. J. Matthews, Evidence for sheet-like auroral ionospheric irregularities, Geophys. Res. Lett., 5, 1039, 1978.

Risbeth, H., and O. K. Garriott, Introduction to Ionospheric Physics, Academic Press, New York, 1969.

Roble, R. G. and M. H. Rees, Time-dependent studies of the aurora: Effects of particle precipitation on the dynamic morphology of ionospheric and atmospheric properties, Planet. Space Sci., 25, 991, 1977.

Rodriguez, P., E. P. Szuszczewicz, D. N. Walker, J. C. Holmes, and M. Singh, The STP/S3-4 satellite experiment: High latitude large scale density irregularities, in Proceedings of the Ionospheric Effects Symposium, edited by J. M. Goodman, F. D. Clarke, and J. Aarons, U.S. Government Printing Office, Washington, DC, 1981.

Singh, M., and E. P. Szuszczewicz, Composite equatorial spread-F wave number spectra from medium to short wavelengths, submitted to J. Geophs. Res., 1983.

Szuszczewicz, E. P., R. T. Tsunoda, R. Narcisi, and J. C. Holmes, Plumex-II: A second set of coincident radar and rocket observations of equatorial spread-F, Geophys. Res. Lett., 8, 803, 1981.

Szuszczewicz, E. P., J. C. Holmes, and M. Singh, The S3-4 ionospheric irregularities satellite experiment: Probe detection of multi-ion component plasmas and associated effects on instability processes, Astrophys. Space Sci., 86, 235, 1982.

Vickrey, J. F., C. L. Rino, and T. A. Potemra, Chatanika/Triad observations of unstable ionization enhancements in the auroral F region, Geophys. Res. Lett., 7, 789, 1980.

Vickrey, J. F., and M. C. Kelley, The effects of a conducting E layer on classical F region cross-field plasma diffusion, J. Geophys. Res., 87, 4461, 1982.

Weber, E. J. and J. Buchau, Polar cap F-layer auroras, Geophys. Res. Lett., 8, 125, 1981.

DISTRIBUTION LIST

DEPARTMENT OF DEFENSE

Assistant Secretary of Defense
COMM, CMD, CONT & INTELL
Washington, DC 20301
01CY ATTN: J. Babcock
01CY ATTN: M. Epstein

Director
Command Control Technical Center
Pentagon RM BE 685
Washington, DC 203011
01CY ATTN: C-650
01CY ATTN: C-312 R. Mason

Director
Defense Advanced Rsch. Proj. Agency
Architect Building
1400 Wilson Blvd.
Arlington, VA 22209
01CY ATTN: Nuclear Monitoring Research
01CY ATTN: Strategic Tech Office

Defense Communication Engineer Center
1860 Wiehle Avenue
Reston, VA 22090
01 CY ATTN: Code R820
01 CY ATTN: Code R410 James W. McLean
01 CY ATTN: Code R720 J. Worthington

Dept. of the Air Force
Headquarters Space Division
(AFSC) Los Angeles Air Force Station
P.O. Box 92960
Los Angeles, CA 90009
01 CY Director, STP,
Col. R. B. Kehl
01 CY Maj. C. Jund
01 CY Lt. Col. J. Sisk
01 CY Capt. J. Dargin

Director
Defense Nuclear Agency
Washington, DC 20305
01 CY H. C. Fitz
01 CY Maj. L.A. Wittwer
01 CY Maj. Ullrich
01 CY Maj. McKechney

Commander
Field Command
Defense Nuclear Agency
Kirtland AFB, NM 87115
01 CY ATTN: FCPR

Director
Interservice Nuclear Weapons School
Kirtland AFB, NM 87115
01 CY ATTN: FCPR

Director
Joint Strat TGT Planning Staff
Offutt AFB
Omaha, NB 68113
01 CY ATTN: JLTW-2
01 CY ATTN: JPST G. Goetz

Joint Chiefs of Staff
Washington, DC 20301
01 CY ATTN: OJC, C35 Evaluation
Office

Commandant
NATO School (SHAPE)
APO New York 09172
01 CY ATTN: U.S. Documents Officer

Under Secretary of Defense
for Research & Engineering
Department of Defense
Washington, DC 20301
01 CY ATTN: Strategic & Space Systems
(OS)

Office of Assistant Secretary of Navy
for Research, Engineering and Systems
Pentagon RM 4D745
Washington, DC 20350
03 CY ATTN: Dr. H. Rabin
Deputy Assistant
Secretary of Navy

Commander/Director
Atmospheric Sciences Laboratory
U.S. Army Electronics Command
White Sands Missile Range, NM 88002
01 CY ATTN: DELAS-EO F. Niles

Commander
Harry Diamond Laboratories
Department of the Army
2800 Powder Mill Road
Adelphi, MD 20783
(CNWDI-inner envelope:
ATTN: DELHD-RBH)
01 CY ATTN: DELHD-TI M. Weiner
01 CY ATTN: DELHD-RB R. Williams
01 CY ATTN: DELHD-NP F. Wimenitz
01 CY ATTN: DELHD-NP C. Moazed

Air Force Office of Scientific Research
Bldg. 410
Bolling Air Force Base
Washington, DC 20332
01 CY ATTN: Lt. Col. T. Cress
01 CY ATTN: H. Radoski

Air Force Global Weather Central
Technical Services Division
Offutt AFB, NE 68113
01 CY ATTN: V. PATTERSON
01 CY ATTN: R. Thompson

Commander
U.S. Army Foreign Science & Tech Ctr.
220 7th Street, NE
Chalottesville, VA 22901
01 CY ATTN: DRXST-SD
01 CY ATTN: R. Jones

Director
U.S. Army Ballistic Research Labs
Aberdeen Proving Ground, MD 21005
01 CY ATTN: Tech Lib Edward Baicy
01 CY ATTN: J. Heimerl

Commander
U.S. Army Satcom Agency
Ft. Monmouth, NJ 07703
01 CY ATTN: Document Control

Commander
U.S. Army Missile Intelligence Agency
Redstone Arsenal, AL 35809
01 ATTN: Jim Gamble

Commander
Naval Electronic Systems Command
Washington, DC 20360
01 CY ATTN: NAVALEX 034 T. Hughes
01 CY ATTN: NAVALEX Code 615
J. A. Koenig
01 CY ATTN: NAVALEX Code 615
R. Thompson
01 CY ATTN: PME 117
01 CY ATTN: PME 117-T
01 CY ATTN: Code 5011
01 CY ATTN: PME-106-T

Commander
Naval Surface Weapons Center
Dahlgren Laboratory
Dahlgren, VA 22448
01 CY ATTN: Code DF-14 R. Butler

Office of Naval Research
Arlington, VA 22217
01 CY ATTN: Code 465
01 CY ATTN: Code 461
01 CY ATTN: Code 402
01 CY ATTN: Code 420
01 CY ATTN: Code 421

Commander
Aerospace Defense Command/DC
Department of the Air Force
ENT AFB, CO 80912
01 CY ATTN: DC Mr. Long

Commander
Aerospace Defense Command/XPD
Department of the Air Force
ENT AFB, CO 80912
01 CY ATTN XPDQQ
01 CY ATTN XP

AF Weapons Laboratory
Kirtland AFB, NM 87117
01 CY ATTN: SUL
01 CY ATTN: CA Arthur H. Guenther
01 CY ATTN: NYTC 1 Lt. Krajci

AFTAC
Patrick AFB, Fl 32925
01 CY ATTN: TF/MAJ Wiley
01 CY ATTN: TN

Air Force Wright Aeronautical Labs
Wright-Patterson AFB, OH 45433
01 CY ATTN: AAD Wade Hunt
01 CY ATTN: AAD Allen Johnson

Deputy Chief of Staff
Research, Development, & ACQ
Department of the Air Force
Washington, DC 20330
01 CY ATTN: AFRDQ

Headquarters
Electronic Systems Division/XR
Department of the Air Force
Hanscom AFB, MA 01731
01 CY ATTN: XR J. Deas

Headquarters
Electronic Systems Division/YSEA
Department of the Air Force
Hanscom AFB, MA
01 CY ATTN: YSEA

Commander
Naval Ocean Systems Center
San Diego, CA 92152
01 CY ATTN: Code 532 J. Richter

Commander
Naval Sea Systems Command
Washington, DC 20362
01 CY ATTN: Capt. R. Pitkin

Commander
Naval Space Surveillance System
Dahlgren, VA 22448
01 CY ATTN: Capt. J. H. Burton

Commander
Naval Air Systems Command
Washington, DC 20360
01 CY ATTN: T. Czuba

Officer-in-Charge
Naval Surface Weapons Center
White Oak, Silver Spring, MD 20910
01 CY ATTN: Code F31

Director
Strategic Systems Project Office
Department of the Navy
Washington, DC 20376
01 CY ATTN: NSP-2141
01 CY ATTN: NSSP-2722 Fred Wimberly

Naval Space System Activity
P.O. Box 96960
Worldway Postal Center
Los Angeles, CA 90009
01 CY ATTN: LCDR V. Gavito
01 CY ATTN: Capt. Brown
01 CY ATTN: Lt. J.M. Winterroth

Headquarters
Electronic Systems Division/DC
Department of the Air Force
Hanscom AFB, MA 01731
01 CY ATTN: DCKC Maj. J.C. Clark

Commander
Foreign Technology Division, AFSC
Wright-Patterson AFB, OH 45433
01 CY ATTN: NICD Library
01 CY ATTN: ETDP B. Ballard

Commander
Rome Air Development Center, AFSC
Griffiss AFB, NY 13441
C1 CY ATTN: Doc Library/TSLD
01 CY ATTN: OSCE V. Coyne

SAMSO/SZ
Post Office Box 92960
Worldway Postal Center
Los Angeles, CA 90009
(Space Defense Systems)
01 CY ATTN: SZJ

Stategic Air Command/XPFS
Offutt AFB, NB 68113
01 CY ATTN: XPFS Maj. B. Stephan
01 CY ATTN: Adwate Maj. Bruce Bauer
01 CY ATTN: NRT
01 CY ATTN: DOK Chief Scientist

OTHER GOVERNMENT

Department of Energy
Albuquerque Operations Office
P.O. Box 5400
Albuquerque, NM 87115
01 CY ATTN: Doc Con for D. Sherwood

Department of Energy
Library Room G-042
Washington, DC 20545
01 CY ATTN: Doc Con for A. Labowitz

Department of Commerce
National Bureau of Standards
Washington, DC 20234
(All Corres. ATTN: Sec. Officer for)
01 CY ATTN: R. Moore

Office of Military Application
Department of Energy
Washington, DC 20545
01 CY ATTN: Doc Con for D. Gale

NASA Headquarters
600 Independence Ave.
Washington, DC 20546
01 CY ATTN: D. Butler
01 CY ATTN: M. Wiskerchen
01 CY ATTN: H. Brinton
01 CY ATTN: J. Lynch

Institute for Telecom Sciences
National Telecommunications & Info. Admin.
Boulder, CO 80303
01 CY ATTN: A. Jean (Unclass only)
01 CY ATTN: W. Utlau
01 CY ATTN: D. Crombie
01 CY ATTN: L. Berry

DEPARTMENT OF DEFENSE CONTRACTORS

Analytical Systems Engineering Corp.
5 Old Concord Rd.
Burlington, MA 01803
01 CY ATTN: Radio Sciences

Berkeley Research Associates, Inc.
P.O. BOX 983
Berkeley, CA 94701
01 CY ATTN: J. Workman

Comsat Laboratories
Linthicum Road
Clarksburg, MD 20734
01 CY ATTN: G. Hyde

Defense Technical Information Center
Cameron Station
Alexandria, VA 22314
02 CY

ESL Inc.
495 Java Drive
Sunnyvale, CA 94086
01 CY ATTN: C. W. Prettie

General Electric Company
Space Division
Valley Forge Space Center
Goddard Blvd King of Prussia
P.O. Box 8555
Philadelphia, PA 19101
01 CY ATTN: M. H. Bortner
Space Science Lab

General Electric Company
P.O. Box 1122
Syracuse, NY 13201
01 CY ATTN: F. Reibert

Institute for Defense Analyses
400 Army-Navy Drive
Arlington, VA 22202
01 CY ATTN: J. M. Aein
01 CY ATTN: Ernest Bauer
01 CY ATTN: Hans Wolfhard
01 CY ATTN: Joel Bengston

HSS, Inc.
2 Alfred Circle
Beford, MA 01730
01 CY ATTN: Donald Hansen

INTL Tel & Telegraph Corporation
500 Washington Avenue
Nutley, NJ 07110
01 CY ATTN: Technical Library

JAYCOR
1401 Camino Del Mar
Del Mar, CA 92014
01 CY ATTN: S. R. Goldman

Lockheed Missiles and Space Co., Inc.
3251 Hanover Street
Palo Alto, CA 94304
01 CY ATTN: Martin Walt, Dept. 52-10
01 CY ATTN: Richard G. Johnson, Dept. 52-12
01 CY ATTN: W. L. Imhof, Dept. 52-12
01 CY ATTN: D. Cauffman
01 CY ATTN: R. Vondrak
01 CY ATTN: J. Reagan
01 CY ATTN: R. Sharp
01 CY ATTN: W. Peterson

Lowell Rsch Foundation, University of
450 Aiken Street
Lowell, MA 01854
01 CY ATTN: K. Bibl
01 CY ATTN: B. Reinisch

Mission Research Corporation
735 State Street
Santa Barbara, CA 93101
01 CY ATTN: P. Fischer
01 CY ATTN: W. F. Crevier
01 CY ATTN: Steven L. Gutsche
01 CY ATTN: D. Sappenfield
01 CY ATTN: R. Bogusch
01 CY ATTN: R. Hendrick
01 CY ATTN: Ralph Kilb
01 CY ATTN: Dave Sowle
01 CY ATTN: F. Fajen
01 CY ATTN: M. Scheibe
01 CY ATTN: Conrad L. Longmire
01 CY ATTN: Warren A. Schleuter

Mitre Corporation, The
P.O. Box 208
Beford, MA 01730
01 CY ATTN: John Morganstern
01 CY ATTN: G. Harding
01 CY ATTN: C. E. Callahan

Mitre Corp.
Westgate Research Park
1820 Dolly Madison Blvd.
McClean, VA 22101
01 CY ATTN: W. Hall
01 CY ATTN: W. Foster

Physical Dynamics Inc.
P. O. Box 3027
Bellevue, WA 98009
01 CY ATTN: E. J. Fremouw

Rand Corporation, The
1700 Main Street
Santa Monica, CA 90406
01 CY ATTN: Cullen Crain
01 CY ATTN: Ed Bedrozian

Riverside Research Institute
80 West End Avenue
New York, NY 10023
01 CY ATTN: Vince Trapani

Sandia Laboratories
P.O. Box 5800
Albuquerque, NM 87115
01 CY ATTN: Doc Con for J. Martin
01 CY ATTN: Doc Con for W. Brown
01 CY ATTN: Doc Con for A. Thornbrough
01 CY ATTN: Doc Con for T. Wright
01 CY ATTN: Doc Con for D. Dahlgren
01 CY ATTN: Doc Con for 3141
01 CY ATTN: Doc Con for Space Project Division

Sandia Laboratories
Livermore Laboratory
P.O. Box 969
Livermore, CA 94550
01 CY ATTN: Doc Con for B. Murphy
01 CY ATTN: Doc Con for T. Cook

Science Applications, Inc.
P.O. BOX 2351
LA Jolla, CA 92038
01 CY ATTN: Lewis M. Linson
01 CY ATTN: Daniel A. Hamlin
01 CY ATTN: D. Sachs
01 CY ATTN: E. A. Straker
01 CY ATTN: Curtis A. Smith
01 CY ATTN: Jack McDoughall

Science Applications, Inc.
80 Mission Drive
Pleasanton, CA 94566
01 CY ATTN: SZ

SRI International
333 Revenswood Avenue
Menlo Park, CA 94025
01 CY ATTN: L. L. Cobb
01 CY ATTN: David A. Johnson
01 CY ATTN: Walter G. Chesnut
01 CY ATTN: Charles L. Rino
01 CY ATTN: R. Livingston
01 CY ATTN: Ray L. Leadabrand
01 CY ATTN: V. Gonzales
01 CY ATTN: D. McDaniel
01 CY ATTN: R. Tsunoda
01 CY ATTN: J. Vickrey

Technology International Corp.
75 Wiggins avenue
Bedford, MA 01730
01 CY ATTN: W. P. Boquist

University of California
Lawrence Livermore Laboratory
P.O. Box 808
Livermore, CA 94550
01 CY ATTN: Doc Con for Tech Info Dept.
01 CY ATTN: Doc Con for L-389 R. Ott
01 CY ATTN: DOC Con for L-31 R. Hager
01 CY ATTN: Doc Con for L-46 F. Seward
01 CY ATTN: FCPRL

UNIVERSITY LIST

Goddard Space Flight Center
Greenbelt, MD 20771
Code 690
N. Ness
R. Stone

Code 692
L. Burlaga
J. Fainberg
M. Goldstein
J. King
A. Klimas
J. Scudder

Code 695
J. Alexander
M. Kaiser
M. Desch
M. Acuna
D. Fairfield
R. Lepping
T. Birmingham
D. Stern

Code 696
R. Hoffman
J. Heppner
T. Aggson
N. Maynard
R. Benson
S. Curtis
L. Brace
J. Grebowsky

Air Force Geophysics Laboratory
Hanscom Air Force Base
Bedford, MA 01731

PHG/ R. Sagalyn
F. Rich
D. Hardy
W. Burke

E. Mullen
D. Knecht
P. Rothwell

P. Fougere
H. Garrett

LKD/ R. Narcisi

PHP/ J. Klobuchar

R. Huffman
H. Carlson
W. Swider

PHD/ J. Buchau
J. Mullen

Los Alamos Scientific Laboratory
P.O. Box 1663
Los Alamos, NM 87545

D. Baker
M. Thomsen
S. P. Gary
J. Gosling
W. Feldman
E. Hones
P. Bernhardt
R. Jeffries
J. Zinn
M. Pongratz
J. Birn
D. Simons

Aerospace Corporation
P.O. Box 92957
Los Angeles, CA 90009

J. Fennel
C. Rice
H. Koons
Y. Chiu
M. Schultz
D. Gorney
D. Chenette
R. Broussard
G. Paulikas
A. Vampola
M. Neudorffer

University of California
Los Angeles
405 Hillgard Ave.
Los Angeles, CA 90024

R. Stenzel
F. Coroniti
C. Kennel
W. Gekelman
C. Russell
J. Luhman
M. Mellott
D. Sentman
M. Kivelson
R. McPherron

Harvard University
Harvard Square
Cambridge, MA 02138

M. McElroy

Pennsylvania State University
University Park, PA 16802

J. Nisbet

University of California
Berkeley
Space Sciences Laboratory
Berkeley, CA 94720

M. Hudson
R. Lin
K. Anderson
F. Mozer
M. Temerin

University of New Hampshire
Space Science Center
Durham, NH 03824

M. Lee
T. Moore
R. Arnoldy
R. L. Kaufmann

University of Iowa
Department of Physics and Astronomy
Iowa City, IA 52242

R. Anderson
L. Frank
D. Gurnett
W. Kurth
N. D'Angelo
J. Van Allen
K. Ackerson
J. Craven
T. Eastman
S. Shawhan
W. Calvert

University of Texas at Dallas
Center for Space Science
P.O. Box 688
Richardson, TX 75080

R. Heelis
W. Heikkila
D. Klumpar
W. Hanson

University of California
San Diego
La Jolla, CA 92093

C. McIlwain
H. Booker
E. Whipple

University of Alaska
Geophysical Institute
Fairbanks, AK 99701

T. Davis
N. Brown
T. Hallinan
D. Swift
S. Akasofu
M. Rees
R. Hunsucker

Boston College
Department of Physics
Chestnut Hill, MA 02167

R. Carovillano
S. Gussenhoven
J. Feynman

John Hopkins University
Applied Physics Laboratory
John Hopkins Road
Laurel, MD 20707

S. Krimigis
D. Williams
T. Potemra
J. Dassoulas
C. Meng
R. Greenwald
B. Mauk

TRW Defense and Space Systems Group
One Space Park
Bldg. R-1
Redondo Beach, CA 90278

R. Fredricks
F. Scarf
E. Greenstadt
W. Taylor

Max Planck Institut Fur Physik
und Astrophysik
8046 Garching B. Munchen
West Germany

Prof. G. Haerendel
Dr. Valenzuela

University of Alabama in Huntsville
Department of Physics
Huntsville, AL 35899

J. Horwitz

Utah State University
UMC 34
Department of Physics
Logan, UT 84322

R. Schunk
J. Sojka
J. Foster
W. Raitt

Jet Propulsion Laboratory
Mail Stop 169
4800 Oak Grove Drive
Pasadena, CA 91104

J. Slavin
B. Tsurutani

National Center for Atmospheric Research
P.O. Box 3000
Boulder, CO 80307

R. Roble
L. House

Space Environment Laboratory
NOAA
Boulder, CO 80303

G. Reed
A. Richmond
Y. Kamide
H. Kroehl
B. Hausman
A. Glenn Jean
G. Adams
D. Anderson
R. Donnelly
R. Grubb
D. Evans
J. Wright

Cornell University
Ithaca, New York 14850

W. Swartz
R. Sudan
D. Farley
M. Kelley
P. Kintner
B. Fejer

Stanford University
Radio Science Laboratory
Standford, CA 94305

R. Helliwell
D. Chang
T. Bell

Marshall Space Flight Center
Space Science Laboratory
Huntsville, AL 35812

A. Dessler
L. Lyons
J. Green
R. Chappell

Southwest Research Institute
P.O. Box 28510
San Antonio, TX 78284

J. Burch
J. Winningham

University of Alberta
Department of Physics
Edmonton, Alberta
CANADA

G. Rostoker

Princeton University
Plasma Physics Laboratory
Princeton, NJ 08540

F. Perkins

University of Maryland
College Park, MD 20742

Dr. K. Papadopoulos
Dr. E. Ott

University of Pittsburgh
Pittsburgh, PA 15213

Dr. N. Zabusky
Dr. M. Biondi

Bell Telephone Laboratories
600 Mountain Ave.
Murray Hill, NJ 07974

L. Lanzerotti

University of Texas at Austin
P.O. Box 8029
Austin, TX 78712

D. Coco

NAVAL RESEARCH LABORATORY

Code 1000 Capt. J. McMorris
Code 1001 T. Coffey
Code 4100 H. Gursky
Code 4101 P. Mange
Code 4006 V. Noble
Code 4190 H. Friedman
Code 4108 E. Szuszczewicz (50 copies)

Code 4120
K. Wood
J. Meekins
G. Fritz
T. Chubb

Code 4130
K. Johnston
S. Knowles

Code 4140
G. Carruthers
R. Meier

Code 4150
J. Kurfess

Code 4160
G. Brueckner

Code 4170
G. Doschek
N. Sheeley
D. Michels
R. Howard

Code 4180
J. Goodman
M. Reilly
F. Kelly

Code 4700
S. Ossakow
J. Brown

Code 4720
J. Davis

Code 4730
S. Bodner
E. McLean

Code 4780
M. Keskinen
P. Palmadesso
J. Huba
J. Fedder
P. Chaturvedi

Code 5000
5300
5700
6000
7000
7500
7580
7551
7555
7700
7900

Code 2628 (20 copies)

END

DATE
FILMED

9 - 83

DTI